Cell Reports
Methods

Article

A flexible and versatile system for multi-color fiber photometry and optogenetic manipulation

Graphical abstract

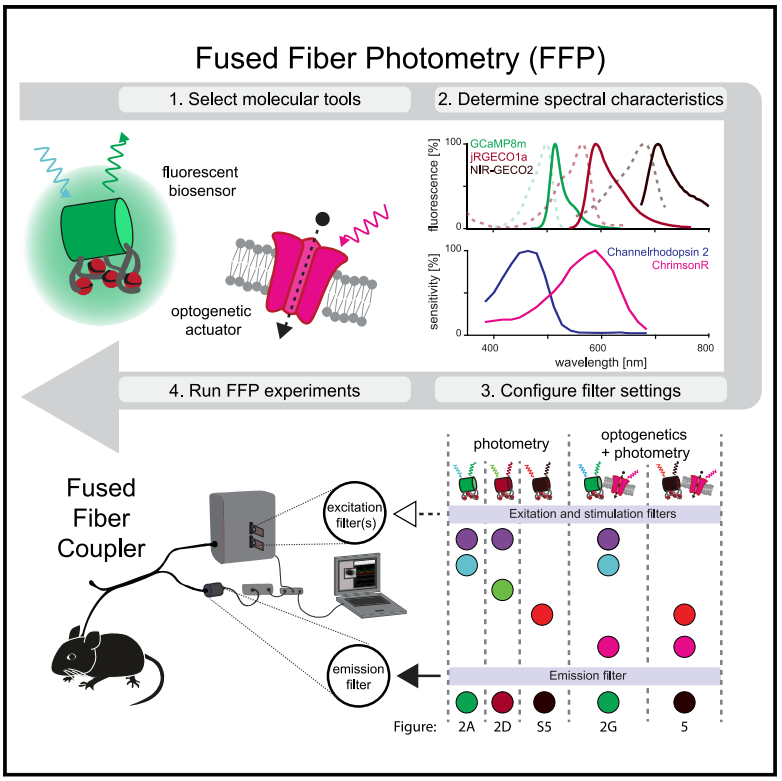

Highlights

- Fused fiber photometry enables monitoring and manipulation of brain activity
- Fluorescent indicators with virtually any spectral characteristics can be used
- Fused fiber photometry is compatible with simultaneous optogenetic manipulation
- Cost-efficient, easy to assemble, and customizable with low effort

Authors

Andrey Formozov, Alexander Dieter, J. Simon Wiegert

Correspondence

simon.wiegert@medma.uni-heidelberg.de

In brief

Formozov et al. present fused fiber photometry (FFP), a simple approach for combined monitoring and control of neuronal activity based on fused fiber couplers. Compared with conventional photometry methods, this approach offers remarkable flexibility in experimental design and facilitates the exploration of new molecular tools *in vivo* at minimal cost.

Formozov et al., 2023, Cell Reports Methods *3*, 100418
March 27, 2023 © 2023 The Author(s).
https://doi.org/10.1016/j.crmeth.2023.100418

CellPress

Cell Reports Methods

CellPress
OPEN ACCESS

Article

A flexible and versatile system for multi-color fiber photometry and optogenetic manipulation

Andrey Formozov,[1,2,3] Alexander Dieter,[1,2,3] and J. Simon Wiegert[1,2,4,*]
[1]Research Group Synaptic Wiring and Information Processing, Center for Molecular Neurobiology Hamburg, University Medical Center Hamburg-Eppendorf, 20251 Hamburg, Germany
[2]Department of Neurophysiology, MCTN, Medical Faculty Mannheim, Heidelberg University, 68167 Mannheim, Germany
[3]These authors contributed equally
[4]Lead contact
*Correspondence: simon.wiegert@medma.uni-heidelberg.de
https://doi.org/10.1016/j.crmeth.2023.100418

MOTIVATION Fiber photometry is a technique of growing popularity in neuroscience. It is mostly used to infer brain activity by recording calcium dynamics in genetically defined populations of neurons. Aside from the wide variety of calcium indicators, other genetically encoded, fluorescent biosensors have recently been engineered to measure membrane potential, neurotransmitter release, pH, or various cellular metabolites, such as ATP or cAMP. However, to freely combine these biosensors with optogenetic actuators in one experiment, pre-configured assemblies of optical hardware are typically needed. Such constraints might hamper a straightforward implementation of new molecular tools, evaluation of their performance *in vivo,* and design of new experimental paradigms, especially if the financial budget is a limiting factor. Hence, a device to flexibly combine molecular tools in different spectral ranges is highly desired.

SUMMARY

Here, we present simultaneous fiber photometry recordings and optogenetic stimulation based on a multimode fused fiber coupler for both light delivery and collection without the need for dichroic beam splitters. In combination with a multi-color light source and appropriate optical filters, our approach offers remarkable flexibility in experimental design and facilitates the exploration of new molecular tools *in vivo* at minimal cost. We demonstrate straightforward re-configuration of the setup to operate with green, red, and near-infrared calcium indicators with or without simultaneous optogenetic stimulation and further explore the multi-color photometry capabilities of the system. The ease of assembly, operation, characterization, and customization of this platform holds the potential to foster the development of experimental strategies for multi-color fused fiber photometry combined with optogenetics far beyond its current state.

INTRODUCTION

Measuring neuronal activity with cellular specificity to understand brain function can be achieved both by electrophysiological and by optical methods. While electrophysiological methods offer high temporal resolution, allowing for direct measurements of neuronal spiking, optical methods have the advantage of retaining spatial information and molecular specificity. The spatial information obtained by optical microscopy techniques allows for chronic imaging of the same structures at cellular and subcellular resolution, including organelles or synapses. However, both of these techniques require expensive, sophisticated equipment, generate enormous amounts of data, and analysis is often complicated. In contrast, fiber photometry measures bulk neuronal activity via an optical fiber. While the temporal resolution of most fluorescent indicators is lower compared to electrical recordings and cellular resolution is lacking, it enables inference of the activity of molecularly defined populations of neurons at very low cost and with straightforward data analysis.[1–3] Epifluorescence miniscope recordings,[4] another technique of increasing popularity, fills an intermediate position between fiber photometry and high-resolution microscopy with regard to spatiotemporal resolution. While providing read-outs at cellular resolution, miniscope recordings are—due to the relatively bulky miniscope itself—typically limited to one recording site and one spectral configuration.[5] In contrast, fiber photometry allows for implantation of several fibers for multi-site, deep brain recordings,[6] and straightforward combination with optogenetic manipulations.[7] Finally, experiments in freely moving animals are easily implementable, as originally demonstrated by Cui et al.[8] Hence, photometry gained increasing popularity in recent years and, despite comparatively low complexity, has

This is an open access article under the CC BY-NC-ND license (http://creativecommons.org/licenses/by-nc-nd/4.0/).

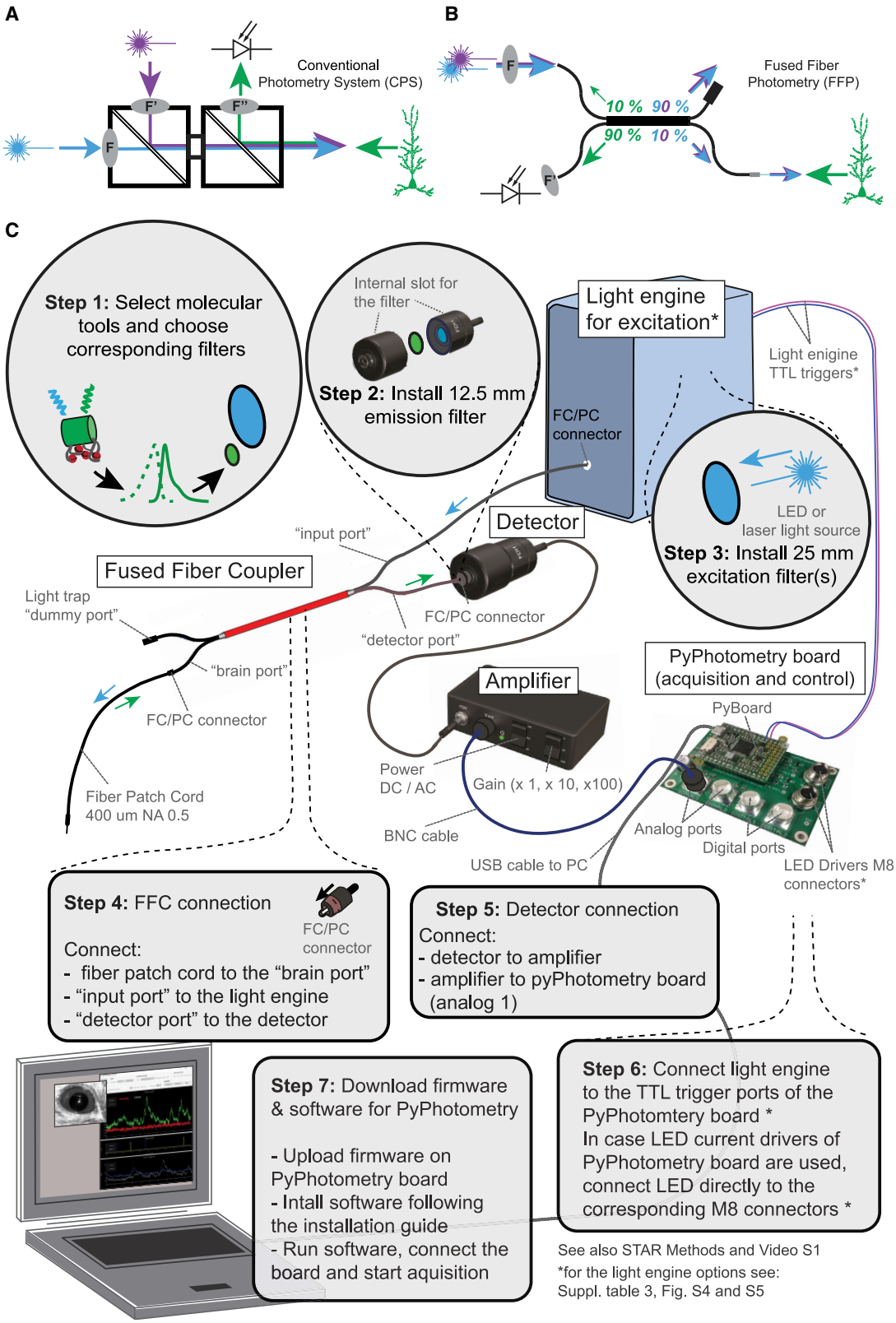

(legend on next page)

substantially contributed to our understanding of brain function.[1,3,9,10]

Capitalizing on the expanding molecular toolbox of genetically encoded fluorescent biosensors, the versatility and applicability of fiber photometry areconstantly increasing. Most indicators so far have been developed for monitoring of intracellular calcium dynamics as a proxy for neural activity.[11] Following the development of the widely used calcium sensor GCaMP[12] and its predecessors, other indicators were engineered to cover a broad color spectrum ranging from blue[13,14] to near-infrared light.[15,16] Additional variants, including FRET-based sensors,[17,18] were developed with different kinetics, affinity, and dynamic range.[19] A more direct way to measure neural activity with millisecond time resolution is offered by genetically encoded voltage indicators.[20,21] Additional sensors were engineered to detect the release of neurotransmitters, including glutamate[22] and γ-aminobutyric acid (GABA),[23] or neuromodulators such as dopamine,[24,25] norepinephrine,[26] acetylcholine,[27] and serotonin.[28] Furthermore, fluorescent sensors are available for many other molecules found in the nervous system, reaching from ATP[29] and cAMP[30] to glucose,[31] lactate,[32] phosphate,[33] magnesium,[34] zinc,[35] and even protons.[36,37] When these new indicators are used in combination, they offer the possibility for multiplexed measurements of various functional parameters in the living brain. On top of monitoring neuronal activity, optogenetic manipulations[38,39] or infrared neural stimulation[40,41] can be added by delivering light of a different spectral range to the brain via the same optical fiber. Similar to optical indicators, a broad spectral palette of optogenetic tools is available for neuronal manipulations.[42,43] Hence, photometric measurements and optogenetic manipulations via a single optical fiber provide a simple and versatile method for bidirectional communication with neural tissue. In combination with anatomically and molecularly specified expression of molecular tools, these technologies hold the potential to tackle previously unaddressed questions of brain function.

While fiber photometry was originally used with a fluorescent calcium-sensitive dye in a single, column-like region of the neocortex,[1] subsequent work has advanced the development of fiber photometry applications in various directions, especially after the introduction of genetically encoded calcium indicators for *in vivo* imaging.[44,45] Later, optical fiber bundles were used to acquire photometry recordings across different brain regions simultaneously, either by distributing excitation light across different fibers with a galvanometer-controlled mirror and collecting the emitted light in a single detector[46] or by imaging the cross-section of the bundle with a camera.[47] The latter approach was further extended with chronically implantable, high-density arrays of optical fibers.[48] Besides monitoring of different brain regions, anatomically intermingled but genetically distinct populations of neurons have been independently measured by spectral separation of green and red calcium[49] and voltage indicators.[50] Another example of the refinement of fiber photometry is the detection of calcium transients in sub-cellular compartments, such as axonal terminals in their target region.[51]

To optimally explore and integrate various combinations of the above-mentioned possibilities for individual experiments, cost-efficient, open-source, and experimentally flexible systems are desired.[52] Recent developments of open-source solutions for fiber photometry have addressed individual aspects of this matter: Control systems and corresponding software to orchestrate optical illumination and signal detection of multiple spectral channels have been developed,[53,54] one of them featuring a graphical user interface written in Python.[53] In a different approach, a customized system based on a lock-in amplifier has enabled fiber photometry recordings at much lower light levels as compared to commercial systems, reducing photobleaching of the biosensor.[55] Furthermore, the combination of fiber photometry recordings with electroencephalogram (EEG) recordings[56] and optogenetic functional magnetic resonance imaging ([o]fMRI)[57] was demonstrated. Finally, open-source analysis platforms have been developed in MATLAB (pMAT[58]) and Python (GuPPy[59]). While all of these efforts greatly reduce costs and increase the accessibility of fiber photometry, they usually lack flexibility. This arises from the fact that the assembly of optical components in current photometry systems was inspired by fluorescence microscopy setups. Thus, they are typically composed of three optical elements to spectrally separate light of different wavelengths: an excitation light filter, an emission light filter, and a dichroic mirror (Figure 1A). For measurements of different indicators with distinct spectra, combination with optogenetics, or multiplexed photometry using multiple indicators in one preparation, the optical assembly needs to be replaced or extended with additional dichroic mirrors and filters, drastically increasing the cost and complexity of the system. However, as photometry records bulk fluorescence and is therefore conceptually simpler than microscopy, the complexity of the setup can be reduced: Instead of dichroic beam splitters, a purely fiber-based approach can be used. The idea of purely fiber-based photometry has recently been realized using a bifurcated optical fiber,[60] and will also be addressed in this manuscript.

Here, we propose a conceptually different type of setup for fiber photometry recordings based on fused optical fibers (fused fiber photometry, FFP). The core of this approach consists of a fused multimode fiber coupler (FFC), simultaneously used for delivery and collection of excitation and emission light, respectively. This coupler can be easily combined with any light source (e.g., transistor-transistor logic [TTL]-controlled lasers or multicolor light-emitting diodes [LEDs] with corresponding clean-up filters) available in most neuroscience labs (e.g., for optogenetic experiments or various imaging approaches) and a sensitive

Figure 1. Fiber photometry recordings realized with a fused fiber photometry (FFP) system

(A) Scheme of a conventional photometry system (CPS) based on excitation and emission filters *F* as well as dichroic mirrors (diagonal lines).

(B) Customized fused fiber coupler for FFP: excitation light delivered in one branch of the coupler (top left) is split into two branches: ~10% is used for the excitation of biosensors, while 90% is dissipated (top right). Emission light from the indicator is collected by the same fiber, 90% of which is guided to the photodetector (bottom left) and cleaned by the optical filter *F'*.

(C) Detailed schematic of a complete FFP system, including assembly instructions.

detector or spectrometer, resulting in a fully operational photometry platform with manifold capabilities. In combination with a small set of optical filters, which can be flexibly exchanged, the FFP platform enables the implementation of novel indicators and actuators for fiber photometry experiments in combination with optogenetic stimulation. This approach broadens the bandwidth of fiber photometry well beyond the possibilities of conventional off-the-shelf setups, which rely on predefined spectral configurations.

RESULTS

FFP: A customizable and flexible platform for light delivery and collection

FFCs are devices commonly used to split optical signals from one fiber into two fibers or, vice versa, combine signals from two fibers into one. These couplers are bidirectional: the same fiber port can be used to deliver excitation light and collect emitted fluorescence (Figure 1B). The splitting ratio of FFCs, i.e., the ratio of light distributed between the two output fibers, is customizable and depends on the length of the fused regions. In this study, we chose an FFC with a fiber diameter of 400 μm, a numerical aperture (NA) of 0.5, and an asymmetrical splitting ratio of 90:10 (for customizations, see Table S1). We have designed an approach to implement FFCs for the recording of *in vivo* fiber photometry signals in the following way: Excitation light is directed into the FFC (Figure 1B, top left), 10 % of which is guided to the brain port in order to excite the biosensor of choice (Figure 1B, bottom right), while 90 % is guided to the dissipation port (Figure 1B, top right). As the FFC preserves the splitting ratio in both directions, light emitted by the biosensor is collected by the brain port. This way, 90 % will be guided to the detector port (Figure 1B, bottom left), while 10% will be lost at the excitation port. In practice, an additional, off-the-shelf patch cord was used to connect the brain port of the FFC to the animal, introducing some coupling losses to the light path. Also, internal losses of the FFC affect light propagation, resulting in an actual light transmittance of ∼8% – 10% in the excitation path and ∼50%– 70% in the emission path, depending on the wavelength (Figure S1). Furthermore, some fraction of excitation light also propagates back to the detector port (∼5% of the power that arrives at the brain port if the brain and dissipation ports are not terminated, or ∼1% with termination by refractive index matching gel). Thus, an emission filter in front of the photodetector is required to avoid contamination of the signal by excitation light (Figure S2). As the excitation light may not be fully monochromatic (e.g., LEDs have a relatively broad spectrum), it can potentially overlap with the band of the emission filter and partially pass through it. In this case, an excitation filter should be installed to clean up any spectral component of the light source that may fall into the transmission bands of the emission filter (Figure S3). As modern, off-the-shelf optical filters provide more than 10^6-fold attenuation, this customization is easy to implement, and it enables the direct use of the FFC for fluorescence detection in a conceptually simpler way as compared with conventional fiber photometry systems, which are built around arrangements of precisely aligned dichroic mirrors and optical filters (Figure 1A). Hence, in combination with an appropriate excitation light source, optical filters, and a photodetector, the FFC becomes a fully functional setup for *in vivo* fiber photometry recordings (Figure 1C), which can easily be adjusted to capitalize on the whole spectrum of available GECIs. The assembly of the FFP system is detailed in sequential steps in Figure 1C, in the STAR Methods section, and in Video S1. For a complete list of components and pricing, see Tables S2 (FFP-hardware), S3 (LED light sources), and S4 (optical filters).

FFP enables recordings of different calcium indicators and combination with optogenetic manipulations *in vivo* with minimal customization

First, we installed optical filters for photometry recordings in the green spectrum: We chose excitation filters at 470/10 nm to excite GCaMP in a calcium-dependent manner and 405/10 nm for excitation of GCaMP near its isosbestic (calcium-insensitive) point. A 530/55 nm emission filter cleaned up the fluorescence (Figure 2A). Data acquisition was performed using the microcontroller-based module of the recently developed, open-source *pyPhotometry* system.[53] We delivered temporally interleaved light pulses at 470 and 405 nm to measure calcium-dependent and -independent fluorescence to control for baseline shifts and motion artifacts.[10,61] We did FFP recordings in awake, head-fixed mice on a linear treadmill by connecting the brain port of the FFC to an animal expressing jGCaMP6s[19] in the CA1 region of the dorsal hippocampus. We observed clear calcium transients with large, positive modulations in the 470-nm channel and slightly negative ones in the 405-nm channel (Figure 2B). Simultaneously, we recorded locomotion and, as a proxy for arousal, pupil diameter. Both arousal and locomotion are correlated with neural activity across a wide range of brain regions (e.g., McGinley et al.[62]), enabling verification of the biological relevance of FFP-signals by their positive correlation to the pupil size and running speed of the animal (Figure 2C). Similar responses, yet with faster kinetics, were observed when using jGCaMP8m[63] (Figures S4A and S4B). We further verified that fluorophore excitation can be achieved with various light sources (e.g., lasers or customized single-color LEDs, as demonstrated in Figures S4 and S5), and is not limited to the commercial, multi-color LED used in this specific setting.

To further demonstrate the versatility of the system, we switched the configuration to record in the red spectrum, using the calcium indicator jRGECO1a[64] expressed in area CA1 of a different animal. In this case, we installed a 575-nm long-pass emission filter and switched the excitation filter for calcium-dependent excitation to 548/10 nm while keeping the 405/10 nm filter for calcium-insensitive excitation[65] to control for artifacts (Figure 2D). Also here, we observed clear calcium transients (Figure 2E) along with a positive correlation to pupil size and running speed (Figure 2F), thus demonstrating functional recordings in the red spectrum.

Next, we combined fluorescent recordings with simultaneous optogenetic stimulation. To this end, we co-expressed jGCaMP8m and the orange-light-activated cation channel ChrimsonR (Chrimson[K176R][42]) in area CA1 of the dorsal hippocampus. To match the activation peak of ChrimsonR (∼590 nm), we used a 575-nm long-pass filter in combination with a 595-nm LED for optogenetic stimulation. In this configuration, we

CellPress
OPEN ACCESS

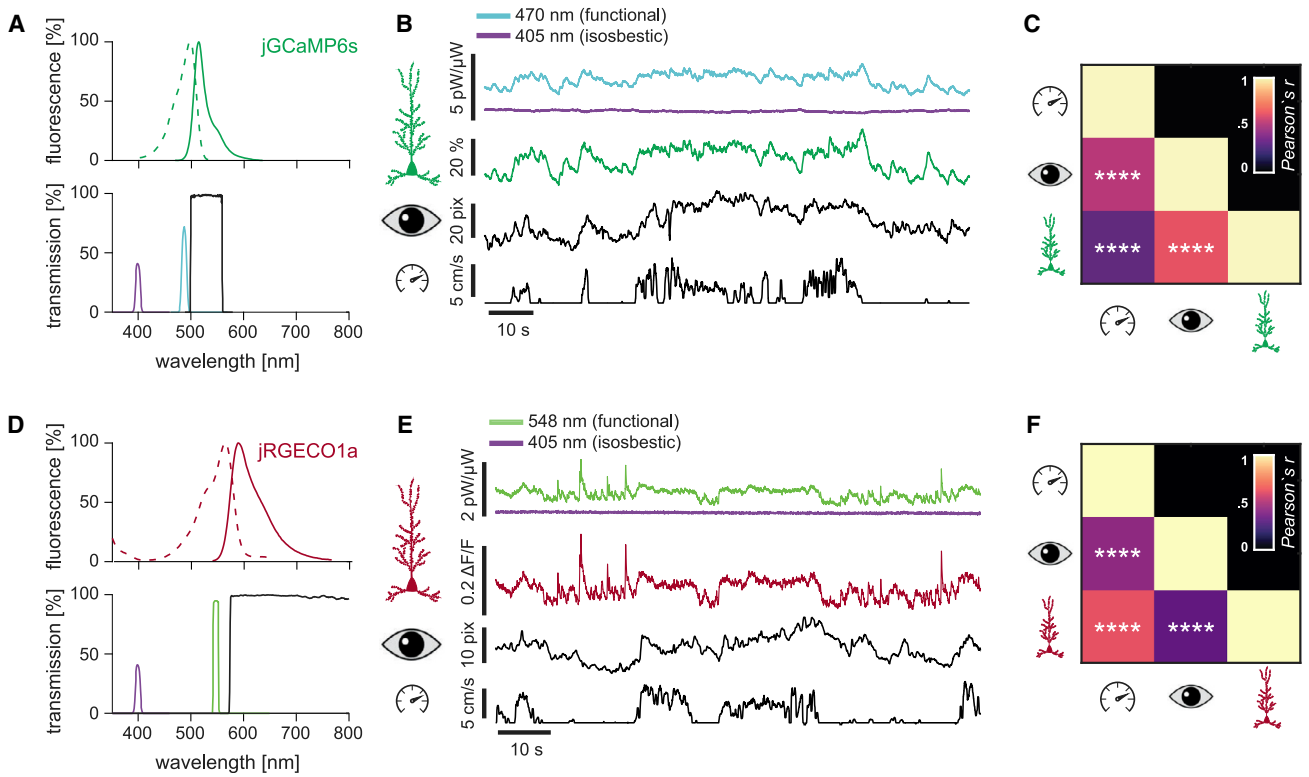

Figure 2. FFP enables flexible photometry recordings in different spectral ranges

(A) Excitation and emission spectrum of jGCaMP6s (top) and properties of excitation (purple and blue) and emission filters (black; bottom).

(B) Top to bottom: representative raw data traces for 470- and 405-nm excitation, corrected calcium signal (ΔF/F), pupil size, and running speed (top to bottom).

(C) Correlation matrix indicating positive correlations between hippocampal calcium activity, pupil size, and running.

(D) Excitation and emission spectrum of jRGECO1a (top) and properties of excitation (purple and green) and emission filters (black; bottom).

(E) Top to bottom: representative raw data traces for 548- and 405-nm excitation, corrected calcium signal (ΔF/F), pupil size, and running speed (top to bottom).

(F) Correlation matrix indicating positive correlations between hippocampal calcium activity, pupil size, and running speed. *r:* Pearson's correlation coefficient*; p:* computed by transforming the correlation to create a t statistic to compare *r* against zero. ****p < 0.0001.

achieved excitation of jGCaMP8m (405 nm, 470 nm) and activation of ChrimsonR (595 nm) via the same FFC, using a single, multi-LED light source (Figure 3A). We verified the absence of signal contamination by ChrimsonR activation light both by spectral recordings of fiber auto-fluorescence with and without illumination from the 595-nm LED using a spectrometer (Figure 3B) and by recordings of auto-fluorescence of the FFC with the photodetector while applying 20 stimuli of 595 light (300 µW, 1-s pulse duration, 0.1-Hz pulse frequency, Figure 3C). We did not detect relevant signal contamination and only observed mild, negligible artifacts when the amplifier gain was increased 100-fold (Figure 3C, bottom). The magnitude of the artifact was only ~0.033 pW per 1 µW of activation light, corresponding to ~0.2% of the typical total signal amplitude (see Table S5), suggesting effective blockage of the activation light by the emission filter and the sampling algorithm in the practically relevant range of fluorescence intensities (usually operating the amplifier at a gain of 1). We then performed recordings from an animal co-expressing jGCaMP8m and ChrimsonR in CA1 while activating this region with optical stimulation (500 µW, 200-ms duration, 0.03 Hz), reliably evoking calcium transients (Figure 3D). The absence of optical artifacts was also verified by the slightly negative response of jGCaMP8m when excited at 405 nm (Figures 3D and 3E) rather than an increase in signal that would be expected as a result of optical cross-talk. Modulating the radiant energy from 0 to 500 µW, we observed that the response strength scaled as a function of stimulus intensity, reaching saturation at ~100 µW (Figure 3F).

In conclusion, we demonstrated that FFP is capable of recording biologically relevant calcium signals *in vivo*. Minimal customization enabled flexible implementation of indicators with different spectral properties and the combination with optogenetic manipulations.

Performance evaluation by comparison with a conventional photometry system

After confirming functionally relevant FFP recordings, we performed a side-by-side comparison of the FFP system against a conventional photometry system (CPS) that is based on dichroic mirrors and mainly assembled from components produced by Doric Lenses.[53] Notably, light detection, data digitization, and acquisition for both systems were performed with the same software and hardware in order to directly compare performance of the different optical assemblies. With both systems, data were

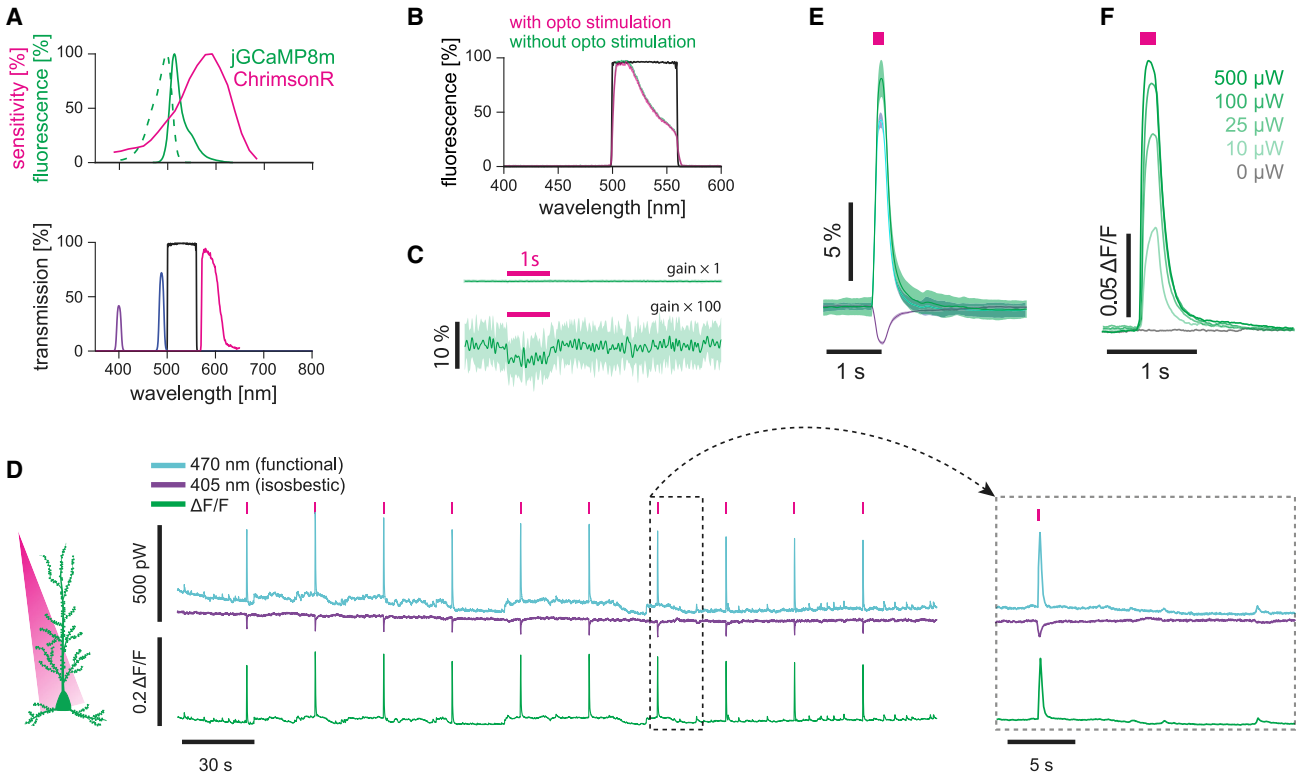

Figure 3. FFP recordings combined with optogenetic stimulation

(A) Spectra of jGCaMP8m and ChrimsonR (top) along with properties of filters for indicator excitation (purple and blue), optogenetic stimulation (magenta), and indicator emission (black; bottom).

(B) Spectrogram indicating the absence of optical contamination by optogenetic stimulation. Transmittance of emission filter (black), spectrum of fiber auto-fluorescence with (magenta) and without (green) simultaneous optogenetic stimulation.

(C) Recording of fiber auto-fluorescence during optogenetic stimulation (300 µW for 1 s: magenta line on top). Stimulation artifacts were not detectable at a gain of 1 (top) and only mildly pronounced at a gain of 100 (bottom). Mean ± standard deviation (STD) of 20 individual traces.

(D) 470 (blue) and 405 nm (purple) excited fluorescence and ΔF/F (green) in response to optogenetic stimulation (500 µW for 0.2 s, stimulation rate 0.03 Hz), indicated by magenta bars. Inset: individual trial.

(E) Mean ± STD of 405-nm excited (purple) and 470-nm excited (blue) fluorescence, as well as ΔF/F (green) of 20 trials of optogenetic stimulation, normalized to stimulus onset (magenta bar).

(F) Average calcium transients in response to optogenetic stimulation with increasing stimulus intensity (20 trials per condition).

acquired from the same three mice co-injected with jGCaMP8m and ChrimsonR in the dorsal hippocampus. While we observed clear differences in the overall signal quality across mice (Figure 4A top to bottom), spontaneous jGCaMP8m-signals were visually comparable between the FFP and the CPS systems (Figure 4A left vs. right). Both approaches revealed comparable calcium transients in the same mice with similar quality-differences across mice. To compare performance in a more controlled and quantitative way, we further recorded optogenetically-evoked calcium transients. To avoid any bias related to signal calculations, we performed this analysis directly on the fluorescence evoked by 470- and 405-nm excitation. Both photometry systems revealed prominent optogenetically evoked responses (Figures 4B and 4C), which were roughly one order of magnitude larger than spontaneous calcium transients. The signal amplitude acquired with the FFP system reached approximately 90% of the signal amplitude that was achieved with the CPS (Figures 4D–4F). Thus, the performance of the FFP system was comparable to a high-quality, commercial system.

Detailed characterization of signal components reveals future directions of FFP development

After benchmarking the FFP against a CPS, we aimed to characterize the composition of the recorded fiber photometry signals to identify possible starting points for future improvements of FFP (see STAR Methods for details). To this end, we used a simple empirical model to quantify the individual components that compose the fluorescence measured at the photodetector: Here, the absolute fluorescence recorded at the photodetector is the sum of sensor fluorescence, auto-fluorescence of the optical fiber, optical implant, and brain tissue, (possible) external background light, as well as non-blocked, backscattered photons of the excitation light (which were negligible, Table S5, Figure 5A). In the first step, we analyzed how the noise of the total signal depends on its amplitude. As it may not be straightforward to study noise characteristics with a sample *in vivo* (due to signal modulations by neuronal activity which differ in each session), we decided to perform these experiments without animals, measuring photodetector noise characteristics with the intrinsic

CellPress
OPEN ACCESS

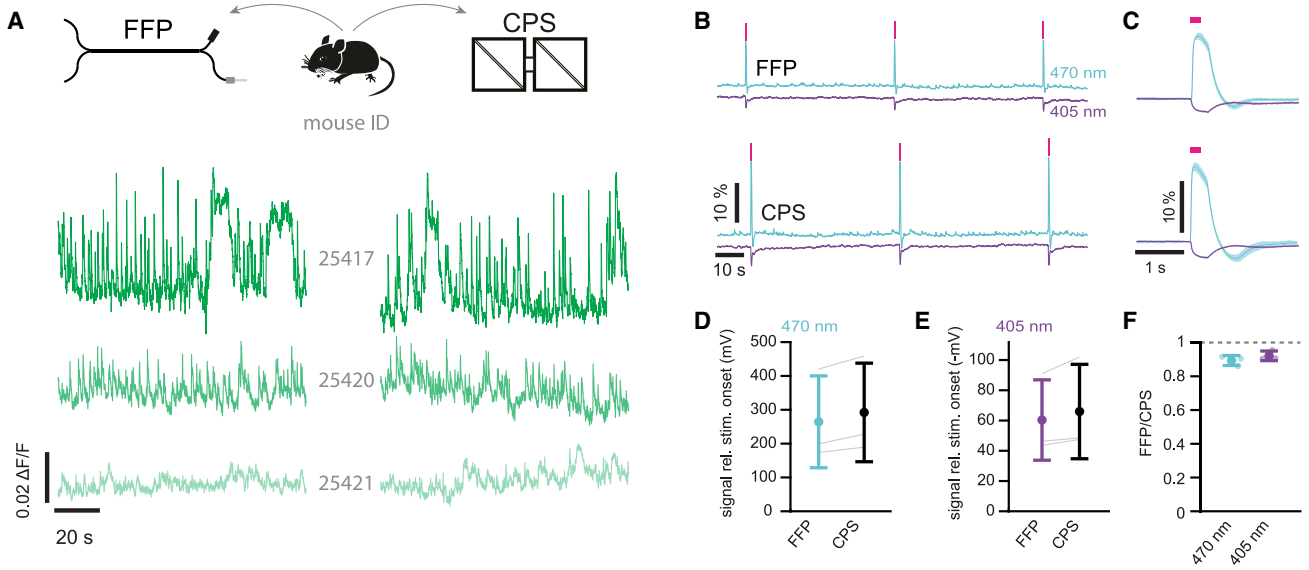

Figure 4. Comparison of FFP to conventional photometry recordings

(A) Spontaneous signals (ΔF/F) in three mice are similar between the FFP (left) and the CPS approach (right).

(B) 470 (blue) and 405 nm (purple) excited raw fluorescence in response to optogenetic stimulation (magenta), recorded with FFP (top) and CPS (bottom).

(C) Mean ± standard deviation (STD) of optogenetically evoked activity when exciting jGCaMP8m at 470 (blue) and 405 (purple) nm recorded with FFP (top) and CPS (bottom). Twenty trials were averaged (solid lines) for each system.

(D and E) The peak amplitude of averaged trials (n = 20) in three different mice (n = 3) when exciting jGCaMP8m at 470 nm (D) or 405 nm (E), recorded with FFP (blue, left) or CPS (black, right). Data is shown as Mean ± STD.

(F) Ratios of FFP vs. CPS-recorded signals when excited at 470 (blue) and 405 nm (purple). Data is shown as Mean ± STD.

fluorescence of the FFC as a reference signal. We observed that the overall standard deviation (STD) of noise linearly increased as a function of signal amplitude, with a constant term (y-axis intercept) of about 0.6 mV (Figure 5B; $STD_{reference\ signal} = 0.54 \times 10^{-3} \times$ Reference Signal +0.55 mV for 470 nm; $STD_{reference\ signal} = 0.69 \times 10_{-3} \times$ Reference Signal +0.64 mV for 405 nm). Yet, the relative measure of the signal-to-noise ratio of the detector, defined as a ratio between the median signal amplitude and the STD of the noise, shows a monotonic increase with saturation at higher signal amplitudes (Figure 5C). Hence, to optimize the signal-to-noise ratio, it is generally advisable to record signals close to the upper limit of the measurable range. In the next step, we analyzed the individual contributions of the signal and found that, by far, the largest contributions originate from fiber and indicator fluorescence, reaching up to ~90% of the total signal (Figure 5D). As a side note, we also found differences in the auto-fluorescence of optical implants manufactured by three companies (Figure 5D, inset). However, as even the implant with the largest auto-fluorescence only mildly contributed to the overall signal, these differences are irrelevant in practice.

These findings have an important implication: one should aim to reduce the intrinsic auto-fluorescence of the FFC in future generations to improve the quality of recordings. By reducing this component of the signal, the overall signal amplitude decreases, consequently also reducing the noise (see Figure 5B) while the amplitude of the relevant biological signals remains unchanged. Indeed, the relative contribution of fiber fluorescence was lower in signals recorded with the CPS (~10%, as compared with ~40% in the FFP system; Figure 5E).

Extending the FFP toolbox to the near-infrared spectrum

After demonstrating the functionality of FFP with commonly used molecular tools and benchmarking it against the conventional approach of fiber photometry recordings, we aimed to exploit the versatility of our system to test novel indicators that have not been commonly used by the community so far. For example, calcium indicators with emission spectra in the near-infrared (NIR) range, namely NIR-GECO[15,66] and iGECI,[16] were recently engineered. However, their performance is still inferior to the established calcium indicators in the field, especially the ones based on cpGFP, and they have not yet found broad application. In addition, the lack of commercial and open-source hardware and costly adaptation of setups to the near-infrared spectrum might also hamper their thorough exploration. Therefore, experimental equipment that easily enables the exploration of novel sensors, such as NIR-calcium indicators, may motivate their further development. Using FFP, the setup can easily be customized to operate with the near-infrared indicator NIR-GECO2, solely requiring a single, additional optical filter (in our case, a 700-nm long-pass filter for emission detection; Figure S6A), which is installed in the photodetector. As the full published excitation spectrum of NIR-GECO2 is calcium sensitive and, therefore, an isosbestic point likely is absent, we excited NIR-GECO2 only in its most calcium-sensitive range with a 650/40 nm bandpass filter, omitting a second spectral excitation band.

Switching the FFP to this configuration, we first estimated the expression of NIR-GECO2 by exciting the indicator in injected mice and compared it with the fluorescence obtained in non-injected wild-type mice: Both the absolute fluorescence

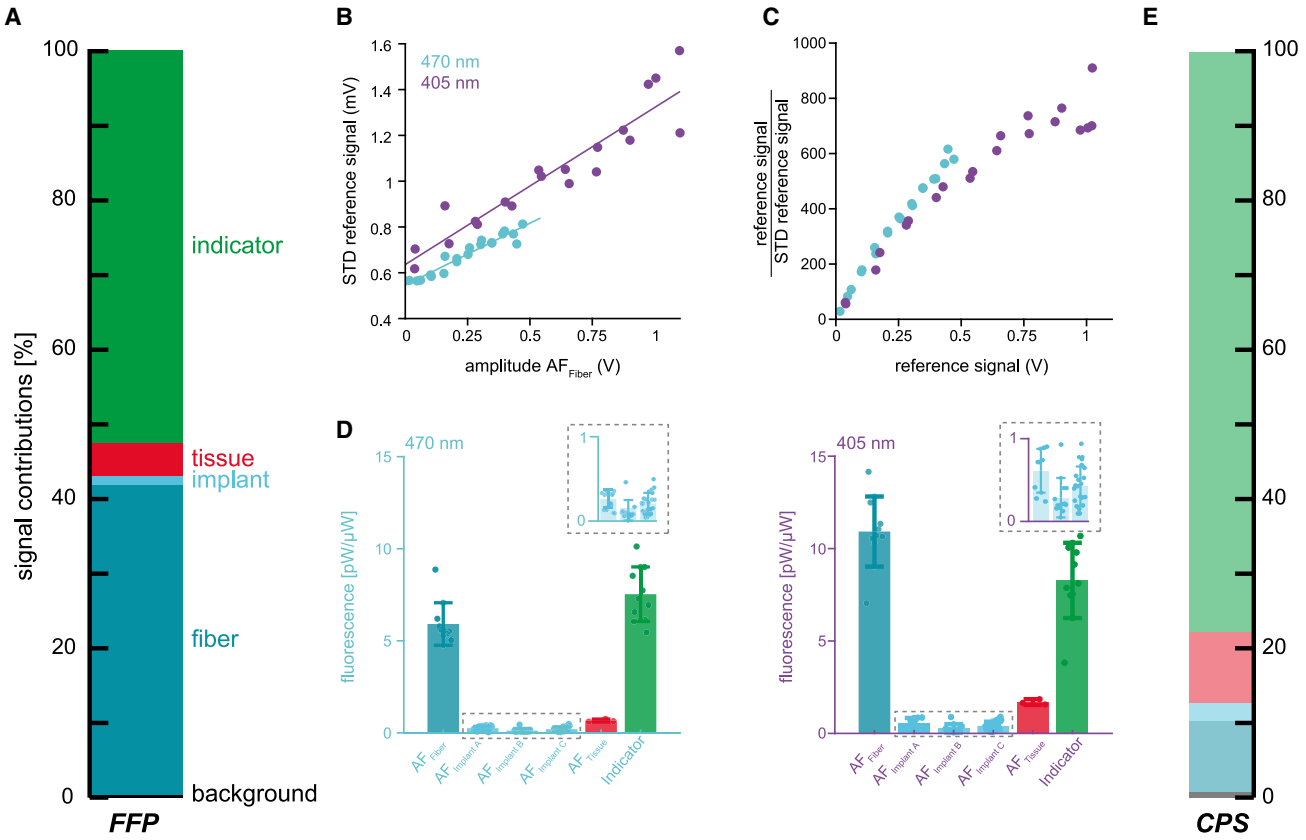

Figure 5. Characterization of signal contributions

(A) Bar graph indicating the relative signal contributions of ambient background light (black), fiber fluorescence (blue), implant fluorescence (light blue), brain tissue (red), and jGCaMP8m (green) to the FFP signal.

(B) Standard deviation (STD) of fiber auto-fluorescence (reference signal) as a function of signal amplitude, exciting the fiber at 470 (blue) and 405 nm (purple).

(C) Amplitude of reference signal divided by its STD as a function of reference signal amplitude.

(D) Fluorescence of different FFP signal components (fiber, implants, native brain tissue, and jGCaMP8m) (from left to right) with excitation light of 470 (blue, left) and 405 nm (purple, right). Inset: zoom in of implant auto-fluorescence by different distributors. Individual data points show independent measurements. Bars show mean ± STD.

(E) Same as (A), but for photometry signals recorded with the CPS.

(Figure S6B) and the bleaching (Figure S6C) were significantly higher in NIR-GECO2 injected mice ($p = 0.007$ and 0.009, respectively; Welch's two-sample t test), indicating successful expression of NIR-GECO2. We then recorded spontaneous NIR-GECO2 activity simultaneously with pupil size and locomotion and observed modulation of NIR-GECO2 fluorescence (Figure S6D). However, as the transients were less prominent than with established indicators and we could not correct the NIR-GECO2 signal for artifacts linked to motion and hemodynamics (which are most likely influenced by arousal and hence linked to pupil size), we could not verify the biological relevance of signal traces with locomotion and pupil size.

To circumvent the uncertainties linked to spontaneous animal behavior, we recorded optogenetically evoked NIR-GECO2 transients by co-expressing ChrimsonR, which can be analyzed in a time-locked fashion. Exploiting the flexibility of the FFP system, we added a 585/22-nm bandpass filter for activation of ChrimsonR to the previous configuration (Figure 6A). Expression of NIR-GECO2 was verified postmortem by confocal microscopy, which revealed a relatively weak fluorescence signal of NIR-GECO2 (Figure 6B). Notably, excitation of NIR-GECO2 at our microscope was not at the maximum of the excitation spectrum (637 nm instead of 678 nm). Furthermore, the calcium-bound state of NIR-GECO2 is dim; hence in fixed cells it is likely that NIR-GECO2 might not be in its bright state due to potentially elevated calcium levels prior to cell death. In some cases, aggregates of NIR-GECO2 were also observed (Figure S6E), suggesting that the expression of NIR-calcium indicators might need further optimization. Despite the seemingly low expression in fixed tissue, optogenetic stimulation resulted in robust NIR-GECO2 transients *in vivo* (Figure 6C). While we could evoke robust transients in every trial in an NIR-GECO2 and ChrimsonR co-expressing animal (Figures 6D and 6E, left), these transients were absent in an animal expressing NIR-GECO2 only (Figures 6D and 6E, center). Instead, we observed a slower and longer-lasting increase in indicator fluorescence, likely reflecting photoconversion of NIR-GECO2 into a fluorescent state of higher brightness. Similar phenomena were reported before

CellPress
OPEN ACCESS

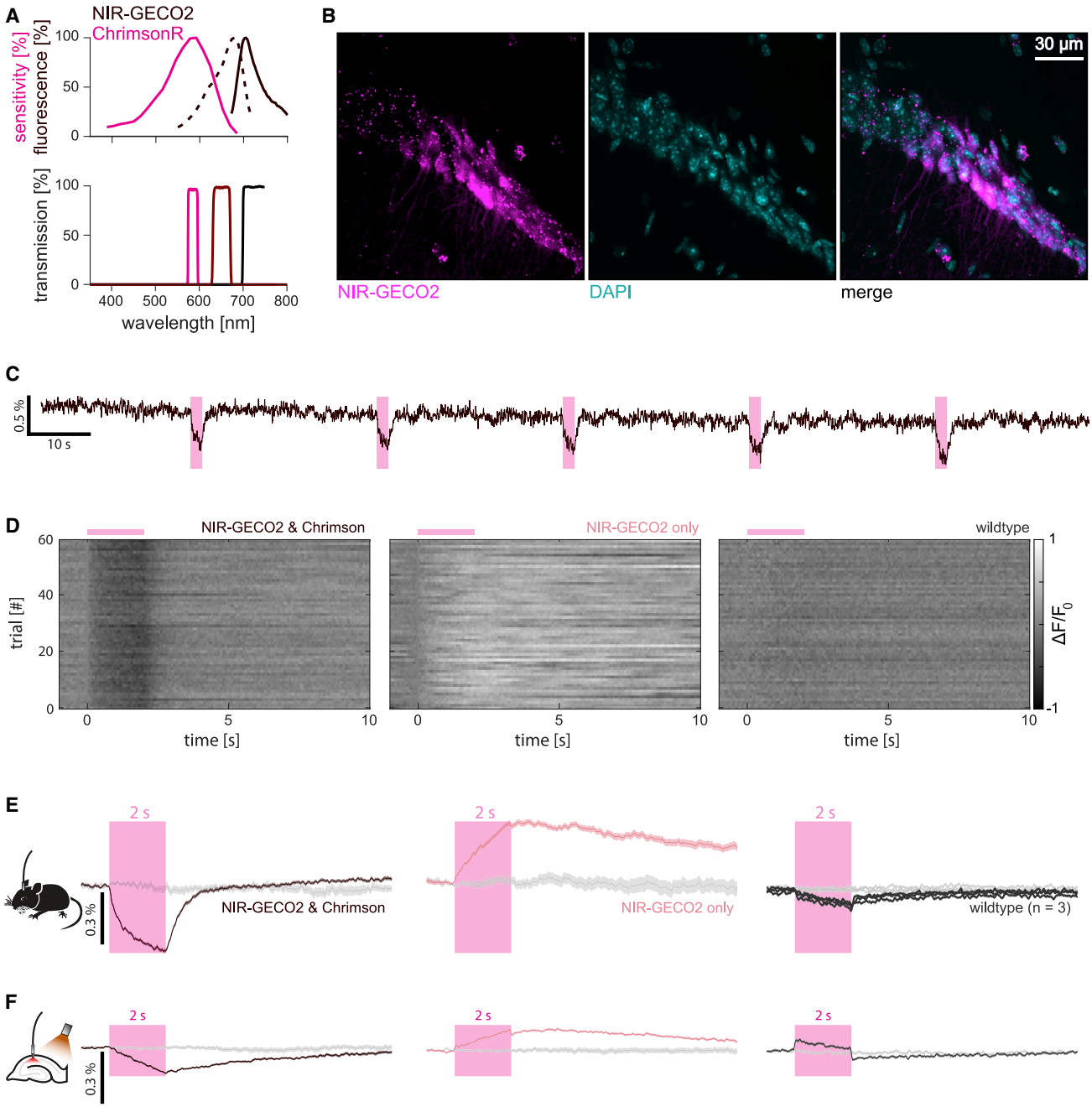

Figure 6. ChrimsonR-evoked calcium responses with fiber photometry recordings of NIR-GECO2

(A) Spectra of NIR-GECO2 and ChrimsonR (top) along with filter properties of excitation (magenta and brown) and emission filters (black; bottom).

(B) Histological verification of NIR-GECO2 expression (magenta) in CA1 hippocampal neurons (cyan: DAPI staining).

(C) Chrimson-evoked (magenta) calcium transients of NIR-GECO2 (bleach-corrected 650 nm functional channel).

(D) $\Delta F/F_0$ of 60 individual trials of stimulation in an animal injected with NIR-GECO2 and ChrimsonR (left), NIR-GECO2 only (center), or without any injection (right).

(E) Mean ± standard error of the mean (SEM) of the traces shown in (D). For the wild-type condition, two additional animals were measured. Gray traces indicate the mean ± SEM of control trials starting at randomly selected time points of the same recording.

(F) *In vitro* experiments in organotypic slice cultures expressing the same constructs as in (E). In these experiments, 595-nm stimulation light was supplied by a separate optical fiber to excite ChrimsonR in the entire slice.

when combining the green-light (560 nm) activated indicator jRGECO1a with an optogenetic actuator activated by shorter wavelengths (i.e., CheRiff, activated at 488 nm).[64,67] To estimate the role of possible optical artifacts, we also performed experiments in wild-type mice that were not injected with any indicator or actuator but only implanted with optical fibers. We observed a minor artifact caused by the activation light, which was one order of magnitude smaller than the responses observed in NIR-GECO2 expressing animals (Figures 6D and 6E, right).

To exclude artifacts caused by *in vivo* preparations (such as breathing, locomotion, or hemodynamics),[10,50,68] we performed analog experiments in organotypic slice cultures transduced with an identical combination of ChrimsonR and NIR-GECO2. While photometry parameters were kept the same, a fiber-coupled laser (594 nm) was used to broadly illuminate the slice for optogenetic stimulation. As before, we observed a decrease in fluorescence when stimulating the slices transduced with NIR-GECO2 and ChrimsonR (Figure 6F, left), while we observed a longer-lasting increase in fluorescence when stimulating NIR-GECO2 in the absence of ChrimsonR (Figure 6F, center). In slices without any transgene expression, we observed stereotyped artifacts with a sharp on- and offset, locked to the optical stimulation (Figure 6F, right). Although the overall magnitude of responses was smaller in organotypic slices as compared with the *in vivo* preparation, these results further verify our conclusions regarding the NIR-GECO2 applicability in combination with a red-light sensitive optogenetic actuator. Overall, these experiments demonstrate the suitability of FFP to explore the usability and limitations of novel genetically encoded sensors, such as calcium indicators in the NIR.

This straightforward technical implementation within the FFP platform opens the door for future experiments using improved versions of NIR-GECO2 or other indicators in the NIR spectrum (such as, for example, the red-light-activated voltage sensors of the QuasAr family[69,70]). Even though the use of these indicators in photometry experiments is not established at this point, it would be highly desirable to measure neuronal activity in the far-red spectrum: This would open the green and red spectrum to other indicators such as the dopamine sensor dLight[71] and the noradrenaline sensor grab-NE.[26] Another example would be the combination with dual-color, bidirectional optogenetic tools, such as BiPOLES[72] or eNPAC2,[73] which only leave a window for photometric measurements in the far-red range.

FFP enables multi-color recordings with minimal customization

As demonstrated above, the combination of temporally interleaved indicator excitation and signal acquisition, together with the choice of an adequate emission filter, enables straightforward customization of the FFP system for experiments (1) involving biosensors of different spectral characteristics, (2) simultaneous recording of a control channel, and (3) combination of biosensors and optogenetic actuators via the same fiber. To fully capitalize on this flexibility, we next aimed to demonstrate the suitability of the FFP system for simultaneous recordings of up to three color channels with different spectral properties showing emission peaks in the green, red, and NIR ranges.

To evaluate the potential and possible drawbacks of multi-color FFP, we first installed a double-bandpass emission filter (514/28–603/55 nm) in the photodetector, enabling simultaneous recordings of two different genetically encoded indicators in the green and in the red range (Figure 7A). Excitation light of 470 nm and 548 nm was delivered in a temporally interleaved manner, enabling temporally, instead of spectrally, separated data acquisition of both indicators with a single photodetector (Figure 7B). We performed FFP recordings in organotypic hippocampal slice cultures expressing the red calcium indicator jRGECO1a and the green norepinephrine indicator grabNE1h.[26] This strategy enabled us to pharmacologically control neuronal calcium dynamics and grabNE1h activation independently with the GABA receptor antagonist bicuculline[74] and norepinephrine, respectively (Figure 7C). Upon bicuculine application, we observed an increase of jRGECO1a fluorescence, followed by high-amplitude oscillations of neuronal activity, indicated by the clear calcium transients detected in the red channel (Figure 7D). We then applied norepinephrine to the slice, leading to a pronounced increase in the fluorescence of grabNE1h in the green channel (Figure 7D). While the green channel demonstrated specific responses to the application of norepinephrine, the presence of mild cross-talk originating from bicuculline-induced rhythmic activity of jRGECO1a, should be noted (Figure 7D). As the excitation spectrum of the jRGECO1a is partially overlapping with the excitation spectrum of grabNE1h, light pulses of 470 nm used for excitation of grabNE1h could, to some extent, also excite jRGECO1a. In contrast, we did not detect contamination of the red channel by the green indicator, as the 550-nm excitation light for jRGECO1a is sufficiently red-shifted with respect to the excitation spectrum of grabNE1h.

In a second set of experiments, we used microscopy slides covered with the fluorophores Alexa 488, Alexa 546, and Alexa 647 (Figure 7E, top), whose emission spectra approximately match those of GCaMP, jRGECO1a, and NIR-GECO2. To this end, we used an off-the-shelf four-bandpass emission filter (440/20521/21–607/34–700/45 nm) (Figure 7E, bottom). As the photodetector used for FFP also enables stacking of different emission filters, the 440/22-nm band, which is irrelevant for this combination of fluorophores, was blocked by an additional 500-nm long-pass emission filter. First, we verified these settings with recordings of the spectral characteristics of the signal obtained from different indicators. Recorded spectra closely matched the reported spectra of fluorophores after the subtraction of the auto-fluorescence background (Figure 7F). Next, we performed temporally interleaved photometry recordings by delivering excitation light of 488/10, 548/10, and 650/10 nm while moving the fused fiber over microscopy slides covered with the fluorophores. Each fluorophore showed a specific response to the corresponding excitation light (as indicated by the arrowheads in Figure 7G).

In conclusion, FFP opens a perspective of temporally interleaved recordings of up to three spectral bands with a single multi-bandpass emission filter—a goal that would require much costlier and more delicate customization with classical fiber photometry setups based on optical channel separation.

CellPress
OPEN ACCESS

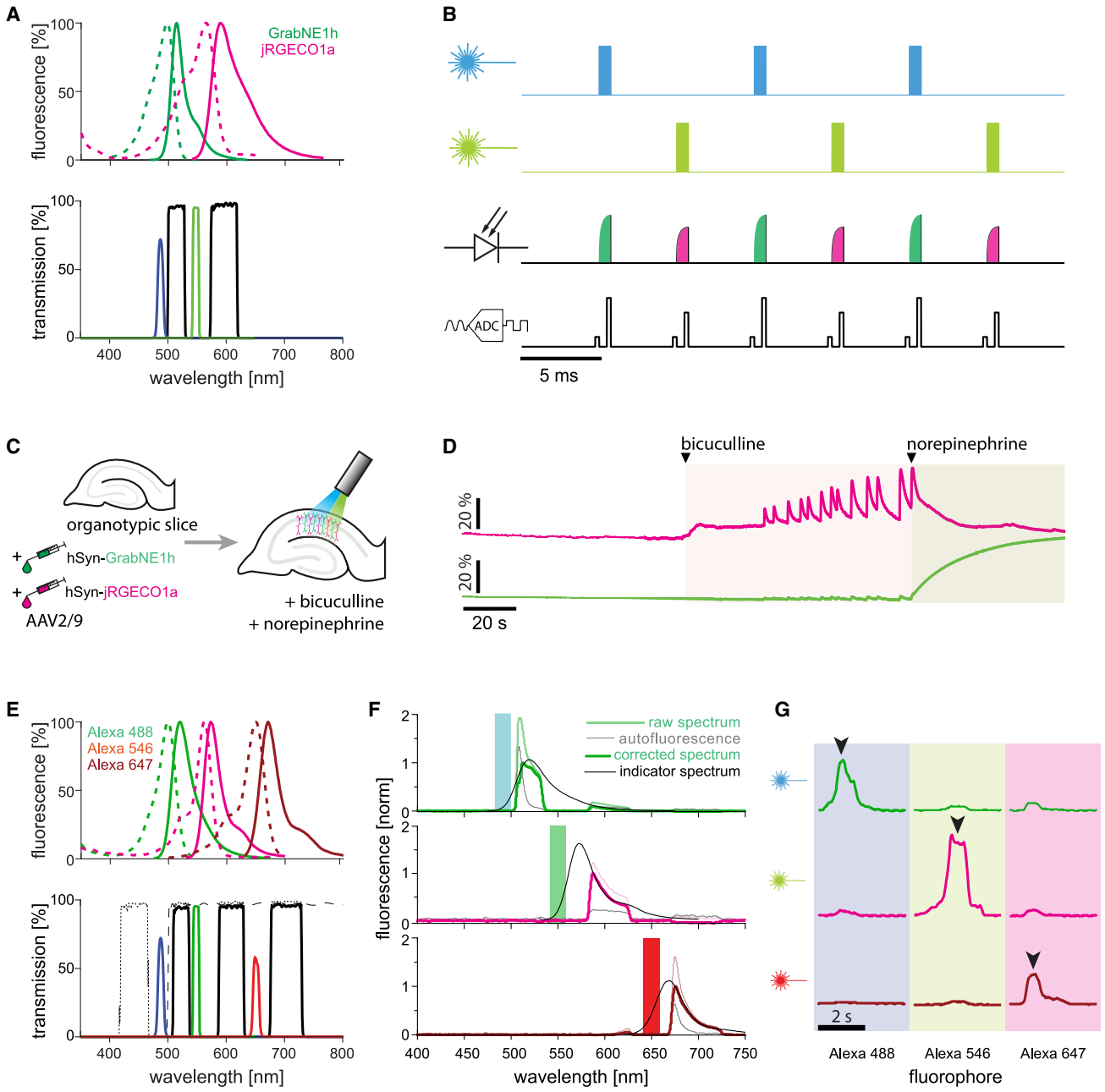

Figure 7. Experimental design and validation of temporally interleaved multi-color FFP recordings

(A) Spectra of GrabNE1h and jRGECO1a (top) along with transmittance of excitation and emission filters (bottom).

(B) Excitation and acquisition scheme: blue and green light pulses are temporally interleaved for respective excitation of a green and a red indicator (top two traces). The fluorescence of the indicator is detected by the same photodetector (third row from top) and digitized by an analog-digital converter in temporally interleaved manner (bottom). For each sampling point, a baseline measurement is taken before the onset of the excitation light (smaller peaks in the bottom trace), which is subtracted from the measurement of the excited state (larger peaks) to correct for background illumination.

(C) Viral transduction of organotypic hippocampal slices with grabNE1h and jRGECO1a.

(D) Bicuculline-induced calcium transients (red), together with the response of grabNE1h to the subsequent application of norepinephrine.

(E) Spectra of Alexa fluorophores, along with transmittance of excitation and emission filters (bottom) for the recording of three spectrally separated signals.

(F) Spectrogram of the triple-color configuration (excitation light of 490, 548, and 650 nm, from top to bottom) using three Alexa fluorophores. Auto-fluorescence spectra (gray lines) are subtracted from the raw spectra (colored thin line) to derive the actual signal of the indicator (corrected spectrum; colored line). Indicator spectra are plotted in black.

(G) The relative intensity of temporally interleaved photometry recordings was achieved with different excitation lights (490, 550, and 650 nm; top to bottom) when pointing the fiber on microscopy slides with Alexa fluorophores.

Thus, the FFP system may significantly broaden the experimenter's toolbox and facilitate the application of novel tools for *in vivo* applications.

DISCUSSION

Here, we propose an innovative concept for fiber photometry recordings based on a multimode fused fiber coupler. Similar approaches for light delivery and collection have previously been used for optical coherence tomography,[75,76] endoscopy,[76,77] temperature sensing,[78] and monitoring of opsin-eGFP expression,[79] but they have not been applied to infer and manipulate neuronal activity. Notably, the flexibility of the FFP system is not limited to the configurations used in this study, as the FFC can efficiently transmit light of any wavelength. This spectral universality is a considerable advantage over conventional dichroic-based systems in terms of flexibility and customization.

Further, we demonstrated the versatility of FFP recordings by the implementation of three different light engines for the delivery of excitation light (a multi-color LED engine, a multi-wavelength laser combiner, and a custom-built dual-color LED system). Establishing the whole setup in a basic configuration matched to the monitoring of green indicators (both with an active and with an isosbestic control channel) can be realized with a budget below 5,000 € (see Table S2). Thus, fiber photometry becomes an accessible research technique also for laboratories with a limited budget.

Combining fiber photometry and optogenetics

The flexibility of the FFP system enables the straightforward addition of optogenetic manipulations. By co-injecting a biosensor along with the opsin, functional modulation of neuronal activity by the opsin can be confirmed, and negative results could be interpreted in a more conclusive way. Negative results of optogenetic modulation in behavioral experiments are currently hard to interpret, as it could have technical (i.e., faulty opsin expression) or biological reasons (i.e., a modulated circuit is indeed not involved in the observed behavior). Furthermore, combining photometry with optogenetics in one device opens the door for closed-looped systems where stimulation is guided by photometry readout.

To this end, the red-shifted opsin ChrimsonR[42] can be combined with GCaMP or NIR-GECO2.[66] We anticipate that exploiting the flexibility of the FFP platform, blue-light-activated opsins such as ChR2,[80] CheRiff,[69] or CatCh[81] can be equally easily combined with red-light-emitting indicators such as jRGECO1a or jRCaMP1.[64] In other studies, optogenetic stimulation and calcium monitoring were achieved by combining blue-light-activated ChR2 with the calcium-sensitive dye OGB-1, which is also excited by blue light and emits green light. As the light power used for optogenetic activation is typically orders of magnitude higher than the photometry excitation light, it can be separated from photometry excitation light by intensity. Moreover, the artifact resulting from optogenetic activation light occurs sharply with the stimulus on- and offset and, therefore, can be separated from the neuronal response in time.[82] Yet, in this case, the problem of the excitation of the green indicator by the blue optogenetic pulse arises and leads to loss of the data points during the optogenetic stimulation. Besides, as always when combining various tools in a single preparation, some effects resulting from specific indicator and opsin properties should be taken into account: For example, when combining a blue-light-gated opsin with the red calcium indicator jRGECO1a, the indicator may be photoconverted into a brighter state by optogenetic stimulation with blue light (which typically exceeds fluorescence excitation light by at least one order of magnitude) and induce changes in the baseline of the calcium indicator as reported before.[64,67] A similar phenomenon was found in this study when combining the near-infrared indicator NIR-GECO2 with the red-light-activated opsin ChrimsonR (Figures 6D–6F). On the other hand, when pairing a green calcium indicator and a red-light-sensitive opsin (e.g., GCaMP and Chrimson), one should be aware that red-shifted opsins typically show some degree of sensitivity to blue light, and the excitation light for the green indicator might interfere with optogenetic stimulation. However, the excitation power used for photometry recordings is typically orders of magnitude lower than the power required for optogenetic stimulation.

Multi-color applications

While we characterized the relevant spectral range of several classical indicators, any combination of excitation and emission spectra could be used if the appropriate filters are installed. However, it is important to note that the bands of the emission filters determine the fraction of the emission spectrum that propagates to the detector when combining different spectral bands in one preparation. Multi-bandpass filters typically have narrower filter bands to accommodate additional bands of excitation light in-between the emission bands (e.g., compare green bands in Figures 2A, 7A, and 7E). Therefore, the gain of additional spectral bands may come at the cost of the signal intensity of other bands. The actual performance of the FFP system for different single- or multi-color configurations can largely be predicted based on the spectral characteristics of the indicator and transmission/blocking characteristics of the filter (for example, using the community editable fluorescent protein database FPbase [https://www.fpbase.org [83]]). Besides enabling multi-color photometry, spectrally resolved photometry[49] could also monitor ratiometric indicators (often consisting of a CFP-YFP pair). To this end, a 430-nm longpass emission filter could be used to cut excitation light for CFP and to capture the full spectral composition of CFP and YFP emission by the spectrometer to determine the FRET ratio.

Future perspectives

From a broader perspective, application of the FFP system is not limited to neuroscientific research, but it can also be used for other excitable cells: For example, tools for simultaneous delivery and collection of light are requested for all-optical readout and control of cardiac activity[84–87] and skeletal muscles.[88] In addition, the conceptual simplicity and potential for miniaturization may be of particular advantage when considering mobile devices, which may enable new applications, including research in freely moving animals or even clinical utilization. Hence, the implementation of fused fiber couplers for optical readout and manipulation of neuronal activity holds great potential for various applications both in basic and in applied research.

CellPress
OPEN ACCESS

Limitations of the study

It is important to note that the commercially available FFCs used in this study were originally not developed to realize photometry recordings but rather to combine light from different sources at a fixed ratio. We exploited that these fused fiber couplers operate in both directions and realized photometry recordings of emitted fluorescence. While the signal quality achieved with the FFP system was sufficient for our experiments, it might reach its limit when biosensors of lower brightness are used, when expression levels are low, when expression occurs only in a small subset of neurons (due to conditional gene expression), or in small brain structures. However, we identified a number of modifications to further improve FFP: First, characterization of signals contributing to the absolute detected fluorescence suggests that the sensitivity of the FFP system is still limited by the auto-fluorescence of several components in the setup. Reducing this fiber auto-fluorescence will (1) result in lower background noise and improve the signal-to-noise ratio at identical excitation power, and (2) enable recordings with higher excitation power, as the auto-fluorescence contribution to the overall signal is decreased. Consequently, the photodetector has a higher dynamic range for sensing indicator fluorescence. If technologically possible, polyimide- and metal-coated fibers can be considered for FFC production as they offer minimal fluorescence.[89]

Second, the efficiency of light collection from the indicator, which depends on the transmittance path to the detector, should be maximized. For optogenetic applications, also the transmittance of the excitation path should be further optimized to achieve a higher radiant flux at the target neural population. Recently, a new fused fiber device, namely a wideband multimode circulator, was reported.[90] This circulator is characterized by higher transmittance of excitation and emission light as compared with the regular fused fiber coupler and hence promises to overcome this problem. Additional parameters affecting the signal (not systematically investigated in this study) are the modal distribution of light in the FFC, launch conditions of light, tracing through the filters and optical junctions, light propagation in the brain, fluorescence emission, and collection efficiencies.[91,92]

Third, customized bandpass filters can be used in future studies in order to optimize both indicator excitation and the collection of light emitted by the indicator. We note that we have not yet succeeded in recording robust signals of two different functional indicators *in vivo*. This was likely due to the relatively high auto-fluorescence of the FFC and the relatively narrow pass-bands of the off-the-shelf filters we have used in this study.

Finally, to circumvent the spectral cross-talk observed in the multi-color setting of the FFP, a fast spectrometer instead of a femtowatt photoreceiver may be used for light detection in multi-color experiments.[49,68] Furthermore, computational methods, such as independent component analysis,[50] might be used for channel separation. However, these methods are not yet commonly used and will need to be established during the future development of the FFP technique.

STAR★METHODS

Detailed methods are provided in the online version of this paper and include the following:

SUPPLEMENTAL INFORMATION

Supplemental information can be found online at https://doi.org/10.1016/j.crmeth.2023.100418.

ACKNOWLEDGMENTS

This work was funded by the Deutsche Forschungsgemeinschaft (DFG, German Research Foundation), SFB 936-178316478-B8 (J.S.W.). A.F. is supported by the Alexander von Humboldt Foundation (AvH Research Fellowship). We thank https://open-ephys.org/ and Thomas Akam for the guidance on pyPhotometry board modifications, and Dr. Maxime Maheu for the adaptation of the pyPhotometry code to accommodate four separate stimulation channels. We thank Adrianna Nozownik for the preparation of organotypic hippocampal slice cultures, Kathrin Sauter for plasmid preparation, Dr. Ingke Braren for virus production, and Stefan Schillemeit for support with histology. We thank Prof. Dr. Thomas Oertner for providing us with the rAAV2/9-hSyn-ChrimsonR(K176R)-mCerulean and rAAV2/10-hSyn-ChrimsonR(K176R)-tdTomato constructs.

AUTHOR CONTRIBUTIONS

Conceptualization, A.F. with the help of A.D. and J.S.W.; methodology, A.F. and A.D.; software, A.F. and A.D; validation, A.F. and A.D; formal analysis, A.F. and A.D; investigation, A.F. (*in vitro*) and A.D. (*in vivo*); data curation, A.F. and A.D.; writing – original draft, A.F. and A.D.; writing – review & editing, all authors; visualization, A.F. and A.D; project administration, J.S.W.; funding acquisition, A.F. and J.S.W.; resources, J.S.W.; supervision, J.S.W.

DECLARATION OF INTERESTS

The authors have a patent application pending for the use of fused fiber optics for bidirectional communication with electrically excitable cells (50%/25%/25% by A.F./A.D./J.S.W.).

Received: March 31, 2022
Revised: December 20, 2022
Accepted: February 8, 2023
Published: March 7, 2023

REFERENCES

1. Adelsberger, H., Garaschuk, O., and Konnerth, A. (2005). Cortical calcium waves in resting newborn mice. Nat. Neurosci. *8*, 988–990. https://doi.org/10.1038/nn1502.
2. Girven, K.S., and Sparta, D.R. (2017). Probing deep brain circuitry: new advances in in vivo calcium measurement strategies. ACS Chem. Neurosci. *8*, 243–251. https://doi.org/10.1021/acschemneuro.6b00307.
3. Wang, Y., DeMarco, E.M., Witzel, L.S., and Keighron, J.D. (2021). A selected review of recent advances in the study of neuronal circuits using fiber photometry. Pharmacol. Biochem. Behav. *201*, 173113. https://doi.org/10.1016/j.pbb.2021.173113.
4. Ziv, Y., Burns, L.D., Cocker, E.D., Hamel, E.O., Ghosh, K.K., Kitch, L.J., El Gamal, A., and Schnitzer, M.J. (2013). Long-term dynamics of CA1 hippocampal place codes. Nat. Neurosci. *16*, 264–266. https://doi.org/10.1038/nn.3329.
5. Resendez, S.L., and Stuber, G.D. (2015). In vivo calcium imaging to illuminate neurocircuit activity dynamics underlying naturalistic behavior. Neuropsychopharmacology *40*, 238–239. https://doi.org/10.1038/npp.2014.206.
6. Martianova, E., Aronson, S., and Proulx, C.D. (2019). Multi-fiber photometry to record neural activity in freely-moving animals. J. Vis. Exp. https://doi.org/10.3791/60278.
7. Li, L., Tang, Y., Sun, L., Rahman, K., Huang, K., Xu, W., Yu, J., Dai, J., and Cao, G. (2017). *In vivo* fiber photometry of neural activity in response to optogenetically manipulated inputs in freely moving mice. J. Innov. Opt. Health Sci. *10*, 1743001. https://doi.org/10.1142/S1793545817430015.
8. Cui, G., Jun, S.B., Jin, X., Pham, M.D., Vogel, S.S., Lovinger, D.M., and Costa, R.M. (2013). Concurrent activation of striatal direct and indirect pathways during action initiation. Nature *494*, 238–242. https://doi.org/10.1038/nature11846.
9. Gunaydin, L.A., Grosenick, L., Finkelstein, J.C., Kauvar, I.V., Fenno, L.E., Adhikari, A., Lammel, S., Mirzabekov, J.J., Airan, R.D., Zalocusky, K.A., et al. (2014). Natural neural projection dynamics underlying social behavior. Cell *157*, 1535–1551. https://doi.org/10.1016/j.cell.2014.05.017.
10. Lerner, T.N., Shilyansky, C., Davidson, T.J., Evans, K.E., Beier, K.T., Zalocusky, K.A., Crow, A.K., Malenka, R.C., Luo, L., Tomer, R., and Deisseroth, K. (2015). Intact-brain analyses reveal distinct information carried by SNc dopamine subcircuits. Cell *162*, 635–647. https://doi.org/10.1016/j.cell.2015.07.014.
11. Baker, P.F., Hodgkin, A.L., and Ridgway, E.B. (1971). Depolarization and calcium entry in squid giant axons. J. Physiol. *218*, 709–755. https://doi.org/10.1113/jphysiol.1971.sp009641.
12. Nakai, J., Ohkura, M., and Imoto, K. (2001). A high signal-to-noise Ca2+ probe composed of a single green fluorescent protein. Nat. Biotechnol. *19*, 137–141. https://doi.org/10.1038/84397.
13. Inoue, M., Takeuchi, A., Manita, S., Horigane, S.I., Sakamoto, M., Kawakami, R., Yamaguchi, K., Otomo, K., Yokoyama, H., Kim, R., et al. (2019). Rational engineering of XCaMPs, a multicolor GECI suite for in vivo imaging of complex brain circuit dynamics. Cell *177*, 1346–1360.e24. https://doi.org/10.1016/j.cell.2019.04.007.
14. Zhao, Y., Araki, S., Wu, J., Teramoto, T., Chang, Y.-F., Nakano, M., Abdelfattah, A.S., Fujiwara, M., Ishihara, T., Nagai, T., and Campbell, R.E. (2011). An expanded palette of genetically encoded Ca2+ indicators. Science *333*, 1888–1891. https://doi.org/10.1126/science.1208592.
15. Qian, Y., Piatkevich, K.D., Mc Larney, B., Abdelfattah, A.S., Mehta, S., Murdock, M.H., Gottschalk, S., Molina, R.S., Zhang, W., Chen, Y., et al. (2019). A genetically encoded near-infrared fluorescent calcium ion indicator. Nat. Methods *16*, 171–174. https://doi.org/10.1038/s41592-018-0294-6.
16. Shemetov, A.A., Monakhov, M.V., Zhang, Q., Canton-Josh, J.E., Kumar, M., Chen, M., Matlashov, M.E., Li, X., Yang, W., Nie, L., et al. (2021). A near-infrared genetically encoded calcium indicator for in vivo imaging. Nat. Biotechnol. *39*, 368–377. https://doi.org/10.1038/s41587-020-0710-1.
17. Miyawaki, A., Llopis, J., Heim, R., McCaffery, J.M., Adams, J.A., Ikura, M., and Tsien, R.Y. (1997). Fluorescent indicators for Ca2+based on green fluorescent proteins and calmodulin. Nature *388*, 882–887. https://doi.org/10.1038/42264.
18. Rose, T., Goltstein, P.M., Portugues, R., and Griesbeck, O. (2014). Putting a finishing touch on GECIs. Front. Mol. Neurosci. *7*, 88. https://doi.org/10.3389/fnmol.2014.00088.
19. Chen, T.-W., Wardill, T.J., Sun, Y., Pulver, S.R., Renninger, S.L., Baohan, A., Schreiter, E.R., Kerr, R.A., Orger, M.B., Jayaraman, V., et al. (2013). Ultrasensitive fluorescent proteins for imaging neuronal activity. Nature *499*, 295–300. https://doi.org/10.1038/nature12354.
20. Jin, L., Han, Z., Platisa, J., Wooltorton, J.R.A., Cohen, L.B., and Pieribone, V.A. (2012). Single action potentials and subthreshold electrical events imaged in neurons with a fluorescent protein voltage probe. Neuron *75*, 779–785. https://doi.org/10.1016/j.neuron.2012.06.040.
21. St-Pierre, F., Marshall, J.D., Yang, Y., Gong, Y., Schnitzer, M.J., and Lin, M.Z. (2014). High-fidelity optical reporting of neuronal electrical activity with an ultrafast fluorescent voltage sensor. Nat. Neurosci. *17*, 884–889. https://doi.org/10.1038/nn.3709.
22. Marvin, J.S., Borghuis, B.G., Tian, L., Cichon, J., Harnett, M.T., Akerboom, J., Gordus, A., Renninger, S.L., Chen, T.-W., Bargmann, C.I., et al. (2013). An optimized fluorescent probe for visualizing glutamate neurotransmission. Nat. Methods *10*, 162–170. https://doi.org/10.1038/nmeth.2333.
23. Marvin, J.S., Shimoda, Y., Magloire, V., Leite, M., Kawashima, T., Jensen, T.P., Kolb, I., Knott, E.L., Novak, O., Podgorski, K., et al. (2019). A genetically encoded fluorescent sensor for in vivo imaging of GABA. Nat. Methods *16*, 763–770. https://doi.org/10.1038/s41592-019-0471-2.
24. Patriarchi, T., Mohebi, A., Sun, J., Marley, A., Liang, R., Dong, C., Puhger, K., Mizuno, G.O., Davis, C.M., Wiltgen, B., et al. (2020). An expanded palette of dopamine sensors for multiplex imaging in vivo. Nat. Methods *17*, 1147–1155. https://doi.org/10.1038/s41592-020-0936-3.
25. Sun, F., Zeng, J., Jing, M., Zhou, J., Feng, J., Owen, S.F., Luo, Y., Li, F., Wang, H., Yamaguchi, T., et al. (2018). A genetically encoded fluorescent sensor enables rapid and specific detection of dopamine in flies, fish, and mice. Cell *174*, 481–496.e19. https://doi.org/10.1016/j.cell.2018.06.042.
26. Feng, J., Zhang, C., Lischinsky, J.E., Jing, M., Zhou, J., Wang, H., Zhang, Y., Dong, A., Wu, Z., Wu, H., et al. (2019). A genetically encoded fluorescent sensor for rapid and specific in vivo detection of norepinephrine. Neuron *102*, 745–761.e8. https://doi.org/10.1016/j.neuron.2019.02.037.
27. Jing, M., Zhang, P., Wang, G., Feng, J., Mesik, L., Zeng, J., Jiang, H., Wang, S., Looby, J.C., Guagliardo, N.A., et al. (2018). A genetically encoded fluorescent acetylcholine indicator for in vitro and in vivo studies. Nat. Biotechnol. *36*, 726–737. https://doi.org/10.1038/nbt.4184.
28. Wan, J., Peng, W., Li, X., Qian, T., Song, K., Zeng, J., Deng, F., Hao, S., Feng, J., Zhang, P., et al. (2020). a genetically encoded GRAB sensor for measuring serotonin dynamics *in Vivo*. Neuroscience). https://doi.org/10.1101/2020.02.24.962282.
29. Arai, S., Kriszt, R., Harada, K., Looi, L.-S., Matsuda, S., Wongso, D., Suo, S., Ishiura, S., Tseng, Y.-H., Raghunath, M., et al. (2018). RGB-color Intensiometric indicators to visualize spatiotemporal dynamics of ATP in single cells. Angew. Chem. Int. Ed. Engl. *57*, 10873–10878. https://doi.org/10.1002/anie.201804304.
30. Harada, K., Ito, M., Wang, X., Tanaka, M., Wongso, D., Konno, A., Hirai, H., Hirase, H., Tsuboi, T., and Kitaguchi, T. (2017). Red fluorescent protein-based cAMP indicator applicable to optogenetics and in vivo imaging. Sci. Rep. *7*, 7351. https://doi.org/10.1038/s41598-017-07820-6.
31. Mita, M., Ito, M., Harada, K., Sugawara, I., Ueda, H., Tsuboi, T., and Kitaguchi, T. (2019). Green fluorescent protein-based glucose indicators report glucose dynamics in living cells. Anal. Chem. *91*, 4821–4830. https://doi.org/10.1021/acs.analchem.9b00447.
32. Barros, L.F., San Martín, A., Sotelo-Hitschfeld, T., Lerchundi, R., Fernández-Moncada, I., Ruminot, I., Gutiérrez, R., Valdebenito, R., Ceballo, S., Alegría, K., et al. (2013). Small is fast: astrocytic glucose and lactate

metabolism at cellular resolution. Front. Cell. Neurosci. *7*, 27. https://doi.org/10.3389/fncel.2013.00027.

33. Gu, H., Lalonde, S., Okumoto, S., Looger, L.L., Scharff-Poulsen, A.M., Grossman, A.R., Kossmann, J., Jakobsen, I., and Frommer, W.B. (2006). A novel analytical method for in vivo phosphate tracking. FEBS Lett. *580*, 5885–5893. https://doi.org/10.1016/j.febslet.2006.09.048.

34. Lindenburg, L.H., Vinkenborg, J.L., Oortwijn, J., Aper, S.J.A., and Merkx, M. (2013). MagFRET: the first genetically encoded fluorescent Mg2+ sensor. PLoS One *8*, e82009. https://doi.org/10.1371/journal.pone.0082009.

35. Lindenburg, L.H., Hessels, A.M., Ebberink, E.H.T.M., Arts, R., and Merkx, M. (2013). Robust red FRET sensors using self-associating fluorescent domains. ACS Chem. Biol. *8*, 2133–2139. https://doi.org/10.1021/cb400427b.

36. Ermakova, Y.G., Pak, V.V., Bogdanova, Y.A., Kotlobay, A.A., Yampolsky, I.V., Shokhina, A.G., Panova, A.S., Marygin, R.A., Staroverov, D.B., Bilan, D.S., et al. (2018). SypHer3s: a genetically encoded fluorescent ratiometric probe with enhanced brightness and an improved dynamic range. Chem. Commun. *54*, 2898–2901. https://doi.org/10.1039/C7CC08740C.

37. Tantama, M., Hung, Y.P., and Yellen, G. (2011). Imaging intracellular pH in live cells with a genetically encoded red fluorescent protein sensor. J. Am. Chem. Soc. *133*, 10034–10037. https://doi.org/10.1021/ja202902d.

38. Boyden, E.S., Zhang, F., Bamberg, E., Nagel, G., and Deisseroth, K. (2005). Millisecond-timescale, genetically targeted optical control of neural activity. Nat. Neurosci. *8*, 1263–1268. https://doi.org/10.1038/nn1525.

39. Yizhar, O., Fenno, L.E., Davidson, T.J., Mogri, M., and Deisseroth, K. (2011). Optogenetics in neural systems. Neuron *71*, 9–34. https://doi.org/10.1016/j.neuron.2011.06.004.

40. Richter, C.-P., Matic, A.I., Wells, J.D., Jansen, E.D., and Walsh, J.T. (2011). Neural stimulation with optical radiation. Laser Photon. Rev. *5*, 68–80. https://doi.org/10.1002/lpor.200900044.

41. Wells, J., Kao, C., Mariappan, K., Albea, J., Jansen, E.D., Konrad, P., and Mahadevan-Jansen, A. (2005). Optical stimulation of neural tissue in vivo. Opt. Lett. *30*, 504–506. https://doi.org/10.1364/OL.30.000504.

42. Klapoetke, N.C., Murata, Y., Kim, S.S., Pulver, S.R., Birdsey-Benson, A., Cho, Y.K., Morimoto, T.K., Chuong, A.S., Carpenter, E.J., Tian, Z., et al. (2014). Independent optical excitation of distinct neural populations. Nat. Methods *11*, 338–346. https://doi.org/10.1038/nmeth.2836.

43. Wiegert, J.S., Mahn, M., Prigge, M., Printz, Y., and Yizhar, O. (2017). Silencing neurons: tools, applications, and experimental constraints. Neuron *95*, 504–529. https://doi.org/10.1016/j.neuron.2017.06.050.

44. Doronina-Amitonova, L.V., Fedotov, I.V., Ivashkina, O.I., Zots, M.A., Fedotov, A.B., Anokhin, K.V., and Zheltikov, A.M. (2013). Implantable fiber-optic interface for parallel multisite long-term optical dynamic brain interrogation in freely moving mice. Sci. Rep. *3*, 3265. https://doi.org/10.1038/srep03265.

45. Lütcke, H., Murayama, M., Hahn, T., Margolis, D.J., Astori, S., Zum Alten Borgloh, S.M., Göbel, W., Yang, Y., Tang, W., Kügler, S., et al. (2010). Optical recording of neuronal activity with a genetically-encoded calcium indicator in anesthetized and freely moving mice. Front. Neural Circuits *4*, 9. https://doi.org/10.3389/fncir.2010.00009.

46. Guo, Q., Zhou, J., Feng, Q., Lin, R., Gong, H., Luo, Q., Zeng, S., Luo, M., and Fu, L. (2015). Multi-channel fiber photometry for population neuronal activity recording. Biomed. Opt Express *6*, 3919–3931. https://doi.org/10.1364/BOE.6.003919.

47. Kim, C.K., Yang, S.J., Pichamoorthy, N., Young, N.P., Kauvar, I., Jennings, J.H., Lerner, T.N., Berndt, A., Lee, S.Y., Ramakrishnan, C., et al. (2016). Simultaneous fast measurement of circuit dynamics at multiple sites across the mammalian brain. Nat. Methods *13*, 325–328. https://doi.org/10.1038/nmeth.3770.

48. Sych, Y., Chernysheva, M., Sumanovski, L.T., and Helmchen, F. (2019). High-density multi-fiber photometry for studying large-scale brain circuit dynamics. Nat. Methods *16*, 553–560. https://doi.org/10.1038/s41592-019-0400-4.

49. Meng, C., Zhou, J., Papaneri, A., Peddada, T., Xu, K., and Cui, G. (2018). Spectrally resolved fiber photometry for multi-component analysis of brain circuits. Neuron *98*, 707–717.e4. https://doi.org/10.1016/j.neuron.2018.04.012.

50. Marshall, J.D., Li, J.Z., Zhang, Y., Gong, Y., St-Pierre, F., Lin, M.Z., and Schnitzer, M.J. (2016). Cell-type-specific optical recording of membrane voltage dynamics in freely moving mice. Cell *167*, 1650–1662.e15. https://doi.org/10.1016/j.cell.2016.11.021.

51. Qin, H., Lu, J., Jin, W., Chen, X., and Fu, L. (2019). Multichannel fiber photometry for mapping axonal terminal activity in a restricted brain region in freely moving mice. Neurophotonics *6*, 035011. https://doi.org/10.1117/1.NPh.6.3.035011.

52. White, S.R., Amarante, L.M., Kravitz, A.V., and Laubach, M. (2019). The future is open: open-source tools for behavioral neuroscience research. Eneuro *6*, ENEURO.0223-19. https://doi.org/10.1523/ENEURO.0223-19.2019.

53. Akam, T., and Walton, M.E. (2019). pyPhotometry: open source Python based hardware and software for fiber photometry data acquisition. Sci. Rep. *9*, 3521. https://doi.org/10.1038/s41598-019-39724-y.

54. Owen, S.F., and Kreitzer, A.C. (2019). An open-source control system for in vivo fluorescence measurements from deep-brain structures. J. Neurosci. Methods *311*, 170–177. https://doi.org/10.1016/j.jneumeth.2018.10.022.

55. Simone, K., Füzesi, T., Rosenegger, D., Bains, J., and Murari, K. (2018). Open-source, cost-effective system for low-light in vivo fiber photometry. Neurophotonics *5*, 025006. https://doi.org/10.1117/1.NPh.5.2.025006.

56. Patel, A.A., McAlinden, N., Mathieson, K., and Sakata, S. (2020). Simultaneous electrophysiology and fiber photometry in freely behaving mice. Front. Neurosci. *14*, 148. https://doi.org/10.3389/fnins.2020.00148.

57. Schmid, F., Wachsmuth, L., Schwalm, M., Prouvot, P.-H., Jubal, E.R., Fois, C., Pramanik, G., Zimmer, C., Faber, C., and Stroh, A. (2016). Assessing sensory versus optogenetic network activation by combining (o)fMRI with optical Ca^{2+} recordings. J. Cereb. Blood Flow Metab. *36*, 1885–1900. https://doi.org/10.1177/0271678X15619428.

58. Bruno, C.A., O'Brien, C., Bryant, S., Mejaes, J.I., Estrin, D.J., Pizzano, C., and Barker, D.J. (2021). pMAT: an open-source software suite for the analysis of fiber photometry data. Pharmacol. Biochem. Behav. *201*, 173093. https://doi.org/10.1016/j.pbb.2020.173093.

59. Sherathiya, V.N., Schaid, M.D., Seiler, J.L., Lopez, G.C., and Lerner, T.N. (2021). GuPPy, a Python toolbox for the analysis of fiber photometry data. Sci. Rep. *11*, 24212. https://doi.org/10.1038/s41598-021-03626-9.

60. Qi, Z., Guo, Q., Wang, S., Jia, M., Gao, X., Luo, M., and Fu, L. (2022). All-fiber-transmission photometry for simultaneous optogenetic stimulation and multi-color neuronal activity recording. Opto-Electron. Adv. *0*, 210081. https://doi.org/10.29026/oea.2022.210081.

61. Dana, H., Sun, Y., Mohar, B., Hulse, B.K., Kerlin, A.M., Hasseman, J.P., Tsegaye, G., Tsang, A., Wong, A., Patel, R., et al. (2019). High-performance calcium sensors for imaging activity in neuronal populations and microcompartments. Nat. Methods *16*, 649–657. https://doi.org/10.1038/s41592-019-0435-6.

62. McGinley, M.J., Vinck, M., Reimer, J., Batista-Brito, R., Zagha, E., Cadwell, C.R., Tolias, A.S., Cardin, J.A., and McCormick, D.A. (2015). Waking state: rapid variations modulate neural and behavioral responses. Neuron *87*, 1143–1161. https://doi.org/10.1016/j.neuron.2015.09.012.

63. Zhang, Y., Rózsa, M., Liang, Y., Bushey, D., Wei, Z., Zheng, J., Reep, D., Broussard, G.J., Tsang, A., Tsegaye, G., et al. (2021). Fast and sensitive GCaMP calcium indicators for imaging neural populations. Neuroscience). https://doi.org/10.1101/2021.11.08.467793.

64. Dana, H., Mohar, B., Sun, Y., Narayan, S., Gordus, A., Hasseman, J.P., Tsegaye, G., Holt, G.T., Hu, A., Walpita, D., et al. (2016). Sensitive red protein calcium indicators for imaging neural activity. Elife *5*, e12727. https://doi.org/10.7554/eLife.12727.

65. Molina, R.S., Qian, Y., Wu, J., Shen, Y., Campbell, R.E., Drobizhev, M., and Hughes, T.E. (2019). Understanding the fluorescence change in red genetically encoded calcium ion indicators. Biophys. J. *116*, 1873–1886. https://doi.org/10.1016/j.bpj.2019.04.007.

66. Qian, Y., Cosio, D.M.O., Piatkevich, K.D., Aufmkolk, S., Su, W.-C., Celiker, O.T., Schohl, A., Murdock, M.H., Aggarwal, A., Chang, Y.-F., et al. (2020). Improved genetically encoded near-infrared fluorescent calcium ion indicators for in vivo imaging. PLoS Biol. *18*, e3000965. https://doi.org/10.1371/journal.pbio.3000965.

67. Nguyen, C., Upadhyay, H., Murphy, M., Borja, G., Rozsahegyi, E.J., Barnett, A., Brookings, T., McManus, O.B., and Werley, C.A. (2019). Simultaneous voltage and calcium imaging and optogenetic stimulation with high sensitivity and a wide field of view. Biomed. Opt Express *10*, 789–806. https://doi.org/10.1364/BOE.10.000789.

68. Zhang, W.-T., Chao, T.-H.H., Yang, Y., Wang, T.-W., Lee, S.-H., Oyarzabal, E.A., Zhou, J., Nonneman, R., Pegard, N.C., Zhu, H., et al. (2021). Spectral fiber-photometry derives hemoglobin-absorption changes for accurate measurement of fluorescent sensor activity. Neuroscience). https://doi.org/10.1101/2021.08.23.457372.

69. Hochbaum, D.R., Zhao, Y., Farhi, S.L., Klapoetke, N., Werley, C.A., Kapoor, V., Zou, P., Kralj, J.M., Maclaurin, D., Smedemark-Margulies, N., et al. (2014). All-optical electrophysiology in mammalian neurons using engineered microbial rhodopsins. Nat. Methods *11*, 825–833. https://doi.org/10.1038/nmeth.3000.

70. Tian, H., Davis, H.C., Wong-Campos, J.D., Park, P., Fan, L.Z., Gmeiner, B., Begum, S., Werley, C.A., Borja, G.B., Upadhyay, H., et al. (2023). Video-based pooled screening yields improved far-red genetically encoded voltage indicators. Nat. Methods. https://doi.org/10.1038/s41592-022-01743-5.

71. Patriarchi, T., Cho, J.R., Merten, K., Howe, M.W., Marley, A., Xiong, W.-H., Folk, R.W., Broussard, G.J., Liang, R., Jang, M.J., et al. (2018). Ultrafast neuronal imaging of dopamine dynamics with designed genetically encoded sensors. Science *360*, eaat4422. https://doi.org/10.1126/science.aat4422.

72. Vierock, J., Rodriguez-Rozada, S., Dieter, A., Pieper, F., Sims, R., Tenedini, F., Bergs, A.C.F., Bendifallah, I., Zhou, F., Zeitzschel, N., et al. (2021). BiPOLES is an optogenetic tool developed for bidirectional dual-color control of neurons. Nat. Commun. *12*, 4527. https://doi.org/10.1038/s41467-021-24759-5.

73. Carus-Cadavieco, M., Gorbati, M., Ye, L., Bender, F., van der Veldt, S., Kosse, C., Börgers, C., Lee, S.Y., Ramakrishnan, C., Hu, Y., et al. (2017). Gamma oscillations organize top-down signalling to hypothalamus and enable food seeking. Nature *542*, 232–236. https://doi.org/10.1038/nature21066.

74. Arnold, F.J.L., Hofmann, F., Bengtson, C.P., Wittmann, M., Vanhoutte, P., and Bading, H. (2005). Microelectrode array recordings of cultured hippocampal networks reveal a simple model for transcription and protein synthesis-dependent plasticity: transcription-dependent neuronal network plasticity. J. Physiol. *564*, 3–19. https://doi.org/10.1113/jphysiol.2004.077446.

75. Lee, B.H., Min, E.J., and Kim, Y.H. (2013). Fiber-based optical coherence tomography for biomedical imaging, sensing, and precision measurements. Opt. Fiber Technol. *19*, 729–740. https://doi.org/10.1016/j.yofte.2013.07.011.

76. Lorenser, D., Quirk, B.C., Auger, M., Madore, W.-J., Kirk, R.W., Godbout, N., Sampson, D.D., Boudoux, C., and McLaughlin, R.A. (2013). Dual-modality needle probe for combined fluorescence imaging and three-dimensional optical coherence tomography. Opt. Lett. *38*, 266–268. https://doi.org/10.1364/OL.38.000266.

77. Lemire-Renaud, S., Rivard, M., Strupler, M., Morneau, D., Verpillat, F., Daxhelet, X., Godbout, N., and Boudoux, C. (2010). Double-clad fiber coupler for endoscopy. Opt Express *18*, 9755–9764. https://doi.org/10.1364/OE.18.009755.

78. Musolino, S., Schartner, E.P., Tsiminis, G., Salem, A., Monro, T.M., and Hutchinson, M.R. (2016). Portable optical fiber probe for in vivo brain temperature measurements. Biomed. Opt Express *7*, 3069–3077. https://doi.org/10.1364/BOE.7.003069.

79. Diester, I., Kaufman, M.T., Mogri, M., Pashaie, R., Goo, W., Yizhar, O., Ramakrishnan, C., Deisseroth, K., and Shenoy, K.V. (2011). An optogenetic toolbox designed for primates. Nat. Neurosci. *14*, 387–397. https://doi.org/10.1038/nn.2749.

80. Nagel, G., Szellas, T., Huhn, W., Kateriya, S., Adeishvili, N., Berthold, P., Ollig, D., Hegemann, P., and Bamberg, E. (2003). Channelrhodopsin-2, a directly light-gated cation-selective membrane channel. Proc. Natl. Acad. Sci. USA *100*, 13940–13945. https://doi.org/10.1073/pnas.1936192100.

81. Kleinlogel, S., Feldbauer, K., Dempski, R.E., Fotis, H., Wood, P.G., Bamann, C., and Bamberg, E. (2011). Ultra light-sensitive and fast neuronal activation with the Ca2+-permeable channelrhodopsin CatCh. Nat. Neurosci. *14*, 513–518. https://doi.org/10.1038/nn.2776.

82. Adelsberger, H., Grienberger, C., Stroh, A., and Konnerth, A. (2014). Vivo Calcium Recordings and Channelrhodopsin-2 Activation through an Optical Fiber. Cold Spring Harb. Protoc. 2014, pdb.prot084145. https://doi.org/10.1101/pdb.prot084145.

83. Lambert, T.J. (2019). FPbase: a community-editable fluorescent protein database. Nat. Methods *16*, 277–278. https://doi.org/10.1038/s41592-019-0352-8.

84. Entcheva, E., and Kay, M.W. (2021). Cardiac optogenetics: a decade of enlightenment. Nat. Rev. Cardiol. *18*, 349–367. https://doi.org/10.1038/s41569-020-00478-0.

85. Entcheva, E., and Bub, G. (2016). All-optical control of cardiac excitation: combined high-resolution optogenetic actuation and optical mapping: all-optical control of cardiac excitation. J. Physiol. *594*, 2503–2510. https://doi.org/10.1113/JP271559.

86. O'Shea, C., Holmes, A.P., Winter, J., Correia, J., Ou, X., Dong, R., He, S., Kirchhof, P., Fabritz, L., Rajpoot, K., and Pavlovic, D. (2019). Cardiac optogenetics and optical mapping – overcoming spectral congestion in all-optical cardiac electrophysiology. Front. Physiol. *10*, 182. https://doi.org/10.3389/fphys.2019.00182.

87. Entcheva, E. (2013). Cardiac optogenetics. Am. J. Physiol. Heart Circ. Physiol. *304*, H1179–H1191. https://doi.org/10.1152/ajpheart.00432.2012.

88. Gundelach, L.A., Hüser, M.A., Beutner, D., Ruther, P., and Bruegmann, T. (2020). Towards the clinical translation of optogenetic skeletal muscle stimulation. Pflugers Arch. *472*, 527–545. https://doi.org/10.1007/s00424-020-02387-0.

89. Utzinger, U., and Richards-Kortum, R.R. (2003). Fiber optic probes for biomedical optical spectroscopy. J. Biomed. Opt. *8*, 121–147. https://doi.org/10.1117/1.1528207.

90. Boudoux, C., Majeau, L., Beaudette, K., and Godbout, N. (2019). Multimode and double-clad fiber couplers for biomedical optics. In Applied Industrial Optics 2019, OSA), p. W2A.3. https://doi.org/10.1364/AIO.2019.W2A.3.

91. Mansy, M.M., Kim, H., and Oweiss, K.G. (2019). Spatial detection characteristics of a single photon fiber photometry system for imaging neural ensembles *. In 2019 9th International IEEE/EMBS Conference on Neural Engineering (NER) (IEEE)), pp. 969–972. https://doi.org/10.1109/NER.2019.8717005.

92. Pisanello, M., Pisano, F., Hyun, M., Maglie, E., Balena, A., De Vittorio, M., Sabatini, B.L., and Pisanello, F. (2019). The three-dimensional signal collection field for fiber photometry in brain tissue. Front. Neurosci. *13*, 82. https://doi.org/10.3389/fnins.2019.00082.

93. Schindelin, J., Arganda-Carreras, I., Frise, E., Kaynig, V., Longair, M., Pietzsch, T., Preibisch, S., Rueden, C., Saalfeld, S., Schmid, B., et al. (2012). Fiji: an open-source platform for biological-image analysis. Nat. Methods *9*, 676–682. https://doi.org/10.1038/nmeth.2019.

94. Taniguchi, H., He, M., Wu, P., Kim, S., Paik, R., Sugino, K., Kvitsiani, D., Fu, Y., Lu, J., Lin, Y., et al. (2011). A resource of cre driver lines for genetic

targeting of GABAergic neurons in cerebral cortex. Neuron *71*, 995–1013. https://doi.org/10.1016/j.neuron.2011.07.026.

95. Bäckman, C.M., Malik, N., Zhang, Y., Shan, L., Grinberg, A., Hoffer, B.J., Westphal, H., and Tomac, A.C. (2006). Characterization of a mouse strain expressing Cre recombinase from the 3' untranslated region of the dopamine transporter locus. Genesis *44*, 383–390. https://doi.org/10.1002/dvg.20228.

96. Gee, C.E., Ohmert, I., Wiegert, J.S., and Oertner, T.G. (2017). Preparation of slice cultures from rodent Hippocampus. Cold Spring Harb. Protoc. *2017*. https://doi.org/10.1101/pdb.prot094888.

97. Binding, J., Ben Arous, J., Léger, J.F., Gigan, S., Boccara, C., and Bourdieu, L. (2011). Brain refractive index measured in vivo with high-NA defocus-corrected full-field OCT and consequences for two-photon microscopy. Opt Express *19*, 4833–4847. https://doi.org/10.1364/OE.19.004833.

STAR★METHODS

KEY RESOURCES TABLE

REAGENT or RESOURCE	SOURCE	IDENTIFIER
Chemicals, peptides, and recombinant proteins		
Bicuculline	Tocris	0130
L-norepinephrine hydrochloride	Merck Millipore	74480
Deposited data		
Raw and analyzed data	This paper	https://doi.org/10.12751/g-node.37lm4m
Experimental models: Organisms/strains		
Mouse: C57BL/6J	Jackson Laboratories	RRID:IMSR_JAX:000664
Rat: Wistar	Janvier Labs	RRID:RGD_13508588
Virus strains		
rAAV2/9-CamKII-GCaMP6s	Chen et al.[19]; *AddGene*	#107790-AAV9
rAAV2/9-hSyn-jRGECO1a	Dana et al.[64]; *AddGene*	100854-AAV9
rAAV2/9-CAG-NIR-GECO2	Qian et al.[66]; *AddGene*, this study	Plasmid 159603; virus N/A
rAAV2/9-hSyn-ChrimsonR-mCerulean	Klapoetke et al.[42]; *AddGene*, this study	Original plasmid 59171; modifications and virus N/A
rAAV2/9-hSyn-jGCaMP8m	Zhang et a.l[63]; *AddGene*	162375-AAV9
rAAV2/10-hSyn-ChrimsonR-tdTomato	Klapoetke et al.[42]; *AddGene*, this study	Plasmid 59171; Virus N/A
Software and algorithms		
MATLAB	Mathworks	RRID:SCR_001622
Python	Python	RRID:SCR_008394
Fiji	Schindelin et al.[93]	RRID:SCR_003070
PyPhotometry code - original	Akam & Walton[53]	https://pyphotometry.readthedocs.io
PyPhotometry code – modified	Maxime Maheu, PhD	https://doi.org/10.6084/m9.figshare.21960050
Scripts to analyze data	This paper	https://doi.org/10.6084/m9.figshare.21915435
Other		
Fused Fiber Coupler	Thorlabs; this paper	TH400R2F2B (customized according to Table S1)
Low-AF, multimode patch cable	Thorlabs	MAF2L1
FC/PC mating sleeve	Thorlabs	ADAFC
Fluorescence detector with amplifier	Doric Lenses	Type DFD_FOA_FC
PyPhotometry board	Open Ephys	RRID:SCR_022940; https://open-ephys.org/pycontrol/pyphotometry
MicroPython pyboard v1.1	Micropython	PYBv1.1
Refractive Index matching gel	Thorlabs	G608N3
Black dust cap	Thorlabs	CAPN
CoolLED LED Illumination System	CoolLED Ltd.	PE-4000
Fiber-coupled LED, 405 nm	Thorlabs	M405FP1
Fiber-coupled LED, 470 nm	Thorlabs	M470F3
T-Cube LED driver	Thorlabs	LEDD1B
Splitter branching fiber optic patch cord	Doric lenses	SBP(2)_200/220/900/900-0.37_1m_FCN-2xZF1.25
Multimode Collimator	Thorlabs	F950FC-A
SM1-threaded adapter	Thorlabs	AD15F

(*Continued on next page*)

CellPress
OPEN ACCESS

Continued

REAGENT or RESOURCE	SOURCE	IDENTIFIER
Lens Tube	Thorlabs	SM1M25
Excitation filter 405/10 nm	Edmund Optics	#65-133
Excitation filter 470/10 nm	Alluxa	SKU: 7394
Excitation filter 548/10 nm	Chroma	ET548/10x
Excitation filter 650/40 nm	Thorlabs,	FBH 650-40
Excitation filter 585/22 nm	Chroma	585/22
Excitation filter 492 nm, short-pass	OptoSigma	SHPF-25C-492
Excitation filter 575 nm, long-pass	Chroma	ET575lp
Emission filter, 530/55 nm	Edmund Optics	#87-736
Emission filter, 700 nm, long-pass	Chroma	ET700LP
Emission filter 514/28-603/55	Chroma	59012m
Emission filter 440/20-521/21-607/34-700/45	Edmund Optics	#87-239
Fiber Optic Patch Cord	Thorlabs	M123L01
Power-meter	Thorlabs	PM40
Spectrometer	Thorlas	CCS200/M
Zirconia mating sleeve	Doric Lenses	SLEEVE_ZR_1.25
Fiber Optic Implant	Doric Lenses	MFC_400/430-0.48_2.0mm_ZF1.25_FLT
Fiber Optic Implant	Thorlabs	CFMLC15L02
Fiber Optic Implant	RWD	R-FOC-L400C-50NA
Super Bond C&B	Sun Medical	K057E

RESOURCE AVAILABILITY

Lead contact

Further information and requests should be directed to the lead contact, J. Simon Wiegert (simon.wiegert@medma.uni-heidelberg.de).

Materials availability

This study did not generate new unique reagents.

Data and code availability

- All data are publicly available at G-Node: https://gin.g-node.org/SW_lab/FusedFiberPhotometry. DOIs are listed in the key resources table.
- All original code is publicly available at Github: https://github.com/SynapticWiringLab/FusedFiberPhotometry. DOIs are listed in the key resources table.
- Any additional information required to reanalyze the data reported in this paper is available from the lead contact upon request.

EXPERIMENTAL MODEL AND SUBJECT DETAILS

Experimental animals

Experiments were performed on 11 mice. Strains were C57BL/J (RRID:IMSR_JAX:000664), *GAD2*-IRES-cre (RRID:IMSR_JAX:028867[94]), and *DAT*-IRES-cre (RRID:IMSR_JAX:006660[95]), as detailed in Table S6. However, all constructs were expressed independent of Cre recombinase, and hence the genetic background was not relevant, as mice were chosen in order to minimize excess in our breeding colonies guided by the principle of the 3Rs (https://nc3rs.org.uk/who-we-are/3rs). Adult mice of either sex between 3 and 8 months of age were used, originating from our in-house colony (~22°C room temperature, ~40% relative humidity, 12/12h light-dark cycle, food and water available *ad libitum*). All experiments were performed in agreement with the German national animal care guidelines and approved by the Hamburg state authority for animal welfare, as well as by the animal welfare officer of the University Medical Center Hamburg-Eppendorf.

Hippocampal organotypic slice cultures

Organotypic hippocampal slices were prepared as in.[96] Brains were explanted from Wistar rats at postnatal day 5–7, and dissected hippocampi were cut into 350 μm slices with a tissue chopper and placed on a porous membrane (Millicell CM, Millipore). Prior to any experimental treatment, the cultures were maintained in the incubator for at least two weeks to mature at 37°C, 5% CO_2 in a medium containing 20% heat-inactivated horse serum (Sigma H1138; supplemented with 1 mM L-glutamine, 0.00125% ascorbic acid, 0.01 mg/mL insulin, 1.44 mM $CaCl_2$, 2 mM $MgSO_4$, and 13 mM D-glucose) in Eagle's Minimum Essential Medium (MEM; Sigma M7278).

METHOD DETAILS

Customization of the fused fiber coupler

The FFC used in this study is based on a commercially available 2 × 2 90:10 step-index multimode fiber optic coupler (TH400R2F2B; with FC/PC connectors, FP400ERT fiber type, Ø400 μm core, NA 0.5; Thorlabs, Germany), for which we have requested up to three custom modifications (see Table S1): (1) The coupler is originally manufactured from a FP400ERT fiber which is characterized by low content of hydroxyl groups (OH). As low OH fibers are characterized by higher absorption – and presumably auto-fluorescence – than high OH fibers (around wavelengths of 400 nm), we have requested the coupler to be produced from a high OH fiber (FP400URT). (2) The second modification was shortening of all FFC branches to 15 cm in order to reduce the total fiber length, and hence the overall fiber auto-fluorescence. A low-auto-fluorescence patch cord (MAF2L1, Thorlabs), together with a FC/PC mating sleeve (ADAFC, Thorlabs), were used to connect the "brain port" of the coupler to the animal. We found that the excitation and emission light propagation is not fully symmetrical in a given device: By measuring the light transmission for all possible combinations of light propagation using different ports as input and output, the configuration with the highest transmittance can be identified to optimize signal quality. Hence, the "brain port" was assigned to the port with the highest transmittance to the 90% portion branch at the opposite side of the coupler, where the emission filter and detector were installed. (3) In an initial, alternative design, a third modification was requested: Here, the brain port was extended from 15 cm to 1 m, and directly terminated in a 1.25 mm ceramic ferrule to connect to the animal. However, this modification abandons the possibility of switching the additional patch cord into patch cords with lower auto-fluorescence. Hence, we subsequently switched to shortened fibers of the FFC, and decided to use off-the-shelf, low-auto-fluorescence patch cords to bridge the brain port to the animal. Furthermore, if the ferrule detaches from the optical fiber due to repeatedly connecting it to the animal, one can simply replace the patch cord, and not the whole fused fiber coupler. The data in Figures 3, 4, 5, S1, S4, and S5E was obtained with the second generation of FFP (i.e., shortened FFC ends and a low-auto-fluorescence patch cord), while data presented in Figures 2, 6, 7, S6, and S7 were obtained with the initial design (i.e., extended brain port directly connected to the animal).

Fused fiber photometry system assembly

In order to turn the FFC into a functional FFP setup, it needs to be equipped with a source for excitation light and a photodetector. The excitation light was provided by a multi-color LED light source (pE-4000; CoolLED, UK), directly coupled to the input port of the FFC (Figure 1B, top left; Figure 1C and Video S1). In this configuration, excitation filters can easily be installed, as the CoolLED (pE-4000) is already equipped with filter holders. Fluorescence was detected with a photodetector system (DFD_FOA_FC; Doric Lenses, Canada) coupled to the detector end (Figure 1B, bottom left; Figure 1C and Video S1). Furthermore, it is recommended to terminate the "dummy end" in a light trap (Figure 1B, top right) in order to reduce backscattering of excitation light. This was achieved by installing an FC/PC mating sleeve (ADAFC; Thorlabs, Germany) filled with refractive index matching gel (G608N3; $n \sim 1.5$ at 402 nm; Thorlabs, Germany) and closed with a black dust cap (CAPN, Thorlabs, Germany). For experiments, the animal was connected to the brain port of the coupler (Figure 1B, bottom right) using a low-auto-fluorescence patch cord coupled to the FFC with an FC/PC mating sleeve. This connection further reduces backscattering from the brain end, as the refractive index of brain tissue has been reported to be ~1.36 in the blue-green spectrum,[97] which is close to the refractive index of the silica core of the fiber ($n \sim 1.46$).

For flexible FFP recordings with different genetically encoded indicators and actuators, adequate excitation and emission filters need to be installed (Figure 1C, steps 1-3). The installation of emission filters is straightforward (Figure 1C, step 2), as the photodetector can be screwed open and is already equipped with optical lenses to ensure close to the perpendicular incidence of emission light on the filter surface (Figure S2). These lenses leave sufficient space for the accommodation of an emission filter between them. As the diameter of the filter slot is slightly larger than the diameter of standard optical filters (12.5 mm), we used a rubber tube (3 mm diameter) wrapped around the filter edges in order to properly center it on the photosensitive area of the detector (Figure S2). Then, we connected all coupler ports to the corresponding connectors of the low-auto-fluorescence fiber patch cord, the light engine and the photodetector (step 4). The photodetector has an external amplifier with three gain settings (x1, x10, x100). In a vast majority of experiments, a gain of 1 was used. The amplifier is connected to the pyPhotometry board via analog 1 port (step 5). The light source state is controlled via TTL trigger pulses delivered by the pyPhotometry board (step 6), which, in turn, is connected to the computer to realize signal acquisition (step 7). Instructions on software installation can be found here: https://pyphotometry.readthedocs.io/en/latest/. A mouse with an optical fiber-based implant is then connected to the fused fiber coupler via the brain port. For further information on setup assembly, see Video S1.

Signal acquisition

Hardware control and data acquisition were realized with a MicroPython pyboard v1.1, with a slightly customized version of the PyPhotometry software uploaded.[53] For control of spectrally separate channels (multi-color photometry or single-color photometry with isosbestic control), the ''single channel time division'' mode of the PyPhotometry-software was used. This mode uses temporally intermingled excitation pulses of alternating wavelengths, and thus the detector is always reading a single channel (the currently excited one) at a time (Figure 7B). The customization of this software was done to perform multi-color experiments and allow control of excitation with up to 4 optical channels and corresponding data acquisition from up to 4 channels from a single photodetector at sampling rates up to 65 Hz (modified by Maxime Maheu, PhD; found at https://github.com/SynapticWiringLab/pyPhotometry, forged from https://github.com/maheump/pyPhotometry, originally developed by Thomas Akam, PhD, https://github.com/pyPhotometry). The analog output channels of the MicroPython board were soldered to BNC connectors and connected to a CoolLED pE-4000 for the generation of excitation light. An analog input channel was connected to the photodetector for signal acquisition and a digital input channel was connected to an externally generated trigger to allow for data synchronization with optogenetic stimulation, pupillometric recordings, and locomotion of the animal on the linear treadmill. To avoid soldering, a PyPhotometry board could be used as an alternative, which is already equipped with connectors for 2 analog and 2 digital channels (distributed by OpenEphys; https://open-ephys.org/pyphotometry-showcase).

Custom light source assembly

If light engines are not already available in the laboratory, a custom light engine can be assembled at low cost in order to realize indicator excitation. This was achieved by combining the output from two commercially available fiber-coupled LED light sources (M405FP1 and M470F3; Thorlabs, Germany) with a Y-shaped combiner (SBP(2)_200/220/900/900-0.37_1m_FCN-2xZF1.25; Doric Lenses, Canada). Fiber-coupled LED light sources can either be powered and controlled by commercial LED drivers (LEDD1B; Thorlabs) or directly by a boosted version of the PyPhotomtery board (for the instructions on PyPhotometry board boosting, see below). The components can be mounted on an aluminum breadboard (MB1530 F/M; Thorlabs) with M6 bolts and M6-M3 screw adaptors for the acquisition board. Assembled custom light engines with commercial LED drivers and with the boosted pyPhotometry board are shown in Figures S4A–S4C and S4D–S4F, respectively. To filter excitation light, a custom filter mount was installed in between the output of the Y-combiner and the input port of the FFC: This filter mount consisted of two multimode collimators (F950FC-A; Thorlabs) installed in SM1-threaded adapters (AD15F; Thorlabs), which were then placed in a lens tube (SM1M25; Thorlabs). The excitation filter is then sandwiched in between these adapters and fixed in the lens tube with two retaining rings to ensure mechanical stability (included with the lens tube SM1M25). The custom light source was combined with a 492 nm short-pass filter (SHPF-25C-492; OptoSigma), as both the 405 nm and the 470 nm light need to pass this excitation filter.

PyPhotometry LED drivers current boost

By design, the PyPhotometry board (version 1.0.2) is equipped with LED drivers and can supply up to 100 mA of current in continuous and time-division modes. We managed to boost the maximum peak current in the time-division mode in the following way: As shown in Figure S5A, we modified the connection of the pyBoard to the USB line by bypassing the redundant diode that causes a voltage drop in the +V power bus and hence limits the performance of the drivers. In accordance with https://pyphotometry.readthedocs.io/en/latest/user-guide/hardware/, the resistance R5 and R6 control the current that flows throughthe LED in the active state. By lowering this resistance, one can increase the current. Hence, we reduced the resistances of the R5 and R6 (Figure S5B) by using additional resistors connected in parallel via available SENSE 1, SENSE 2 and GND pins. We found that a resistance of 0.47 Ohm is sufficient to achieve a 10-fold increase of the peak current while maintaining the linearity of the scale and preventing saturation (Figures S5C and S5D). The short-term stability of the pulses was also verified (Figure S5E). When implementing these changes, it is advisable to consult the corresponding online resources for the most recent hardware updates.

System characterization

After the assembly of the FFC system, a characterization of its optical properties was performed. To this end, we have coupled the CoolLED pE-4000 to an optical fiber (200 μm diameter, 0.5 NA) and measured the output power at all available wavelengths with a power meter (PM40; Thorlabs, Germany). We then connected this fiber to the input port of the FFC and measured the output power obtained at the brain end. The transmittance was then calculated as the ratio between the power measured at the brain end and the input power from the light-delivering fiber (Figures S1A–S1C). Transmittance of the emission path of the fused fiber coupler was measured in a similar way, but this time the light was delivered via a photometry patch cord (400 μm diameter, 0.5 NA) directly connected to the CoolLED pE-4000 at the FC end, and coupled into the brain end of the fused fiber coupler via a zirconia mating sleeve (SLEEVE_ZR_1.25; Doric lenses, Canada) to emulate fluorescence emitted by the biosensor, while the power of transmitted light was measured at the detector end of the fused fiber coupler (Figures S1D–S1F). For the comparison of the FFP system with a conventional photometry system, we recorded data from the same 3 mice with both systems. As both systems have different levels of intrinsic auto-fluorescence, we assessed this auto-fluorescence before each recording session and subtracted it from the acquired data.

Signal characterization

Next, we used a simple empirical model to quantify the individual components which compose the fluorescence measured at the photodetector (Figure 4). Here, the absolute fluorescence (F) recorded at the photodetector is the sum of several components, namely sensor fluorescence (F_{Sensor}, which can be further split into baseline fluorescence and ligand-modulated fluorescence), auto-fluorescence of the optical fiber (F_{Fiber}), optical implants ($F_{Implant}$) and brain tissue (F_{Tissue}), non-blocked back-scattered photons of the excitation light (F_{Ex}), as well as (potential) external background light sources in proximity to the photometry setup ($f_{Background}$) and residual light from simultaneous optogenetic stimulation (f_{Opto}). Mathematically, this model is summarized by a simple equation:

$$F = F_{Sensor} + F_{Fiber} + F_{Implant} + F_{Tissue} + F_{Ex} + f_{Background} + f_{Opto}$$

As all signal contributions (except the background light $f_{Background}$) are proportional to the power of excitation light, it is convenient to normalize all recorded signals to excitation power, obtaining a ratio between the signal level at the detector end, and the excitation power at the fiber tip of the brain end [V/μW]. The recorded voltage can then be converted into fluorescence [nW/μW] using the characteristics of the photodetector (the conversion ratio for the photodetector used in this study is 0.76 V for 1 nW of light power at 550 nm). This conversion factor is wavelength-dependent and monotonically increases for longer wavelengths in the range 400–900 nm. For convenience, we have used the same conversion factor across the whole range of light used in this study. These values, normalized to the excitation power can provide useful guidance during troubleshooting and comparisons across different experimental settings, indicators, and setups. Here, we perform a detailed characterization and discuss individual signal contributions for excitation using 405/10 and 470/10 nm when recording emitted light at 530/55 nm, a setting suitable for the recording of green fluorescence, which covers the spectrum of most commonly used indicators (Table S5).

Optical fibers generate intrinsic auto-fluorescence (F_{Fiber}). This auto-fluorescence depends on the material of the multimode fiber core and cladding and on the distribution of guided light modes (with higher modes undergoing more absorption and reemission processes). The contribution of the auto-fluorescence F_{Fiber} may dominate the signal in the case of low biosensor expression levels or dim biosensors. Hence, it is generally advisable to reduce F_{Fiber} to a minimum, e.g., by photobleaching: As we demonstrated for the most commonly used wavelengths, photobleaching (using a laser light source at 405, 470, 595, and 630 nm; ~50 mW each, for 12 h) can reduce the auto-fluorescence - and hence its contribution to the absolute signal F - around 10-fold for excitation light of 405 and 470 nm and ~2.5-fold for excitation light of 550 nm (Figure S7). In absolute terms, the fused fiber coupler showed remaining fiber auto-fluorescence, F_{Fiber}, of ~10.9 and 5.9 pW/μW for 405 nm, 470 nm, respectively (measured with an emission filter of 530/55 nm; Edmund Optics, Stock #87-736). Similarly, we analyzed the auto-fluorescence of optical fiber-based implants fromthree different manufacturers (Thorlabs, Doric lenses, RWD). We found $F_{Implant}$ to amount to 0.58, 0.27, and 0.38 pW/μW when exciting at 405 nm, and 0.27, 0.12, and 0.15 pW/μW when exciting at 470 nm. Despite these differences, it is important to note that all of these contributions were at least one order of magnitude lower than the signal contributions of F_{Fiber}, and hence contributed much less to the overall signal quality.

Beyond fiber and implant auto-fluorescence, also the auto-fluorescence of biological tissue (F_{Tissue}) contributes to the overall signal in a tissue-specific manner. Here, we have measured the auto-fluorescence of live brain tissue of three non-injected wildtype mice with optical fibers implanted into the hippocampus in the same way as we have estimated F_{Fiber} and $F_{Implant}$, but subtracting the fiber auto-fluorescence from the measured signal (Table S5).

Another source of possible signal contamination are backscattered photons of excitation light (F_{Ex}). In our system, F_{Ex} is the sum of backscattered photons from all fiber surfaces which propagate to the detector end, mainly originating from the empty dissipation (“dummy”) and brain ends of the coupler (and presumably from the coupler fusion interface). F_{Ex} amounts to 5.5 and 5% of the used excitation light of 405 and 470 nm, respectively. As the backscattering at the fiber ends originates from the difference in refractive indices of the fiber and the medium surrounding it, it can be reduced by ~ 2-fold (2.4/2.4% for 405/470 nm, respectively) by covering the dissipation end of the fused fiber coupler with refractive index matching gel. Additional coverage of the brain end with refractive index matching gel (emulating an experimental setting in which the brain end is terminated by brain tissue) further decreased the proportion of backscattered light to 1.2/1.1% for 405/470 nm, respectively. Finally, F_{Ex} is drastically attenuated by the use of an adequate emission filter. Modern filters guarantee an optical density (OD) > 6, defined as $OD = \log_{10}(100\%/T\ [\%])$, which gives more than a million-fold suppression of backscattered excitation light in the blocking region. In our case, this results in an overall signal contribution of 0.02/0.01 pW per μW excitation light (Table S5), which is negligible in comparison to F_{Fiber}, $F_{Implant}$, and F_{Tissue}.

Ambient light sources may also induce signal contamination, which we denote as $f_{Background}$. In the current version of the system, the data acquisition was performed with a time-binned technique developed by Akam and colleagues[53]: This technique relies on excitation light pulses of 0.75 ms duration, flanked by brief signal acquisition periods from the photodetector. The signal preceding the excitation pulse measures contribution from the background light in the experimental room and is then subtracted from the signal following the excitation pulse (that contains the sum of the desired signal and background contribution). This way, components of $f_{Background}$, which are usually of lower frequency than the signal acquisition, are effectively canceled out (for a more detailed description, see Akam & Walton[53]), and hence $f_{Background}$ is compensated. Nonetheless, we have also assessed the background light contribution by recording signals in animals without excitation light delivered, which amounted to 5 ± 0.3 pW in our experimental setting. In contrast to other signal components, $f_{Background}$ depicts a constant and does not scale with the excitation light. Thus, the relative contribution of $f_{Background}$ becomes smaller with increasing excitation power in an experimental setting. Like backscattering light, $f_{Background}$ is significantly reduced by an appropriate emission filter that fully blocks external light outside the indicator emission band.

If photometry and optogenetics are combined, the emission filter should be chosen to maximally block the light of optogenetic stimulation. Residual contamination (f_{Opto}) may still contribute to the signal, inducing an artifact during illumination. However, this artifact is efficiently circumvented by the same algorithm that subtracts background light from other sources (for details, see data acquisition).

Finally, the main component contributing to the absolute fluorescence is the light emitted by the biosensor, F_{Sensor}, which is a combination of baseline fluorescence and actual ligand-modulated fluorescence. Both components critically depend on the type of indicator and its characteristics, and are typically assessed and reported during the characterization of a novel indicator (e.g., Figure 2 in Dana et al.,[61] for the GCaMP-family). However, it is important to note that these features are usually measured by cross-calibration of fluorescence microscopy with patch-clamp recordings in single neurons, and their extrapolation to *in vivo* photometry is not trivial, as (i) photometry signals contain activity from all neuronal compartments, and (ii) minimum fluorescence (in the absence of calcium influx) cannot be reached in the living brain. In our experiments (with mice expressing GCaMP8m under the control of the human synapsin promoter in CA1 of the hippocampus) F_{Sensor} amounted to 8.3 and 7.5 pW/μW, when excited at 405 and 470 nm, respectively. However, the exact contribution of F_{Sensor} in different experiments depends on indicator brightness, dynamic range, expression level, and distribution in the tissue. Thus, F_{Sensor} may or may not exceed other background contributions in individual experiments, and should be determined for each experimental setting.

Surgical procedures

All surgical procedures were performed under general anesthesia, either achieved by an intraperitoneal injection of a cocktail containing Midazolam, Medetomidine, and Fentanyl (MMF; 5.0, 0.5, and 0.05 mg/kg, respectively, diluted in NaCl), or by inhalation of Isoflurane (5% for induction, ~1.5% for maintenance), and anesthetic depth was confirmed by the absence of the hindlimb withdrawal reflex. Adequate analgesia was achieved with intraperitoneal injections of Buprenorphine (0.1 mg/kg in NaCl) in the case of Isoflurane anesthesia. During anesthesia, animals were placed on a heating pad to maintain body temperature, and eye ointment (Vidisic; Bausch + Lomb, Germany) was applied to prevent drying of the eyes. The scalp of the animal was then shaved and disinfected by application of Iodide solution (Betaisodona; Mundipharma, Germany), and the animal was fixed in a stereotactic frame. To access the brain region of interest, a small incision (~1 cm) was made along the scalp, and the skull was cleaned from any remaining tissue before bregma and Lambda were stereotactically aligned. A small craniotomy (~0.5 mm) was then performed over the region of interest (2 mm posterior and 1.5 mm lateral to bregma to access CA1 of the hippocampus) using a dental drill. A glass pipette filled with viral suspension was then slowly lowered into the CA1 region of dorsal hippocampus (−1.6 mm relative to bregma) using a micromanipulator. After a minute, viral suspension was slowly injected into the tissue at a speed of ~100 nL/min by using a custom-made, manual air pressure system until a total volume of 500–600 nL was applied. After completion of the injection, the micropipette was kept in place for at least 1 min before it was slowly retracted. To monitor calcium-modulated fluorescence across different wavelengths, we injected either rAAV2/9 encoding GCaMP6s[19] under the control of the CaMKII promoter (1.25×10^{13} gc/ml; *AddGene* viral prep #107790-AAV9; kindly gifted by James M. Wilson), rAAV2/9 encoding jGCaMP8m[63] under the control of the human Synapsin promoter (1×10^{13} gc/ml; *AddGene* viral prep #162375-AAV9; kindly gifted by the GENIE project), rAAV2/9 encoding jRGECO1a under the control of the human synapsin promoter (4×10^{13} gc/ml; customized from *AddGene* plasmid #100854; kindly gifted by Douglas Kim & GENIE Project[64]), or rAAV2/9 encoding for NIR-GECO2 under the control of the synthetic CAG promoter (0.5×10^{12} - 1×10^{13} gc/ml; *AddGene* plasmid #159603; kindly gifted by Robert Campbell[66]). For optogenetic activation, we injected either rAAV2/10 encoding ChrimsonR(K176R) and the red fluorophore tdTomato under the control of the human synapsin promoter (1.13×10^{13} gc/ml; *AddGene* plasmid #59171; kindly gifted by Edward Boyden[42]) or rAAV2/9 encoding ChrimsonR(K176R) and the cyan fluorophore mCerulean under the control of the human synapsin promoter (1.5×10^{12} gc/ml; customized from *AddGene* plasmid #59171; kindly gifted by Edward Boyden[42]). A detailed list of animals and viruses used in the different experiments is provided in Table S6. Upon virus injection, ferrule-coupled optical fibers (2 mm length, 400 μm diameter, 0.5 NA, CFMLC15L02; Thorlabs, Germany) were slowly inserted at the same coordinates to a depth terminating 100-200 μm above the injection site and fixed to the roughened skull using cyanoacrylate glue (Pattex; Henkel, Germany) and dental cement (Super Bond C&B, Sun Medical, Japan). 5% charcoal powder was mixed with the powder of the dental cement in order to reduce optical artifacts. In addition, a head post (200-200 500 2110; Luigs-Neumann, Germany) was fixed to the skull using dental cement to allow for animal fixation during the experiments before the incised skin was fixed to the cement with cyanoacrylate glue to close the surgical site. Once the dental cement hardened, the situs was disinfected by Iodide solution, and anesthesia was antagonized by an intraperitoneal injection of a cocktail containing Atipamezole, Flumazenil, and Buprenorphine (2.5, 0.5, and 0.1 mg/kg, respectively, diluted in NaCl) in the case of MMF-mediated anesthesia. Additional analgesia was then provided by subcutaneous injection of Carprofen (4 mg/kg, diluted in NaCl), and Meloxicam was mixed into softened food for the three days following surgery.

FFP recordings *in vivo*

Experiments were performed earliest 3 weeks after surgical procedures to allow for animal recovery, subsidence of potential inflammations, and sufficient transgene expression. Initially, animals were handled for a couple of minutes on 2-3 subsequent days to allow for habituation to the experimenter before being taken to the setup. Subsequently, animals were habituated to head fixation (200-100 500 2100; Luigs-Neumann, Ratingen, Germany) on a linear treadmill (700-100 100 0010; Luigs-Neumann, Ratingen, Germany) for increasing amounts of time in subsequent sessions. Once animals stayed calm on the treadmill, we recorded spontaneous calcium

activity, locomotion, and videography of the animal's eye as follows: The fiber tip (brain end) of FFC was connected to the ferrule of the optical fiber implant on the animals' head using a zirconia mating sleeve (SLEEVE_ZR_1.25; Doric lenses, QC, Canada) and covered with a black shrinking tube to reduce optical noise. Excitation of biosensors was achieved using a multi-LED illumination system (pE-4000; CoolLED, Andover, UK) with appropriate ⌀25 mm clean-up filters: 405/10 nm OD4 (#65-133, Edmund Optics), 470/10 nm OD4 (7394, Alluxa), 548/10 nm OD6 (ET548/10x, Chroma), at intensities of 50–200 μW at the brain end. Photodetector readout and data digitization was realized with our modified version of the pyPhotometry system,[53] using a time-binned sampling mode with baseline subtraction at a sampling rate of 65–130 Hz. In short, background illumination was measured in a time interval of 250 μs using a commercial fluorescence detector (DFD_FOA_FC; Doric lenses, QC, Canada). Subsequently, biosensors were excited with a light pulse of 750 μs duration, while the emitted light was measured in the last 250 μs of the excitation period. The difference between the excited state and the baseline was then taken as the intensity of light emitted by the biosensors. Mouse locomotion was measured from treadmill movement with a commercial virtual reality system, while the virtual reality displays were not operated (700-100 100 0010; Luigs-Neumann, Ratingen, Germany). Finally, the animal's eye was monitored using a monochrome camera (DMK 33UX249; The Imaging Source, Germany) with a macro objective (TMN 1.0/50; The Imaging Source, Germany) and a 780 nm long-pass filter (FGL780; Thorlabs, Germany). Background illumination at 850 nm was provided by an infrared spotlight, while baseline pupil dilation was adjusted to be moderate using a UV-LED coupled into a polymer fiber and directed to the animal's eye. Measurements were synchronized by custom scripts written in MATLAB (The MathWorks; Nattick, US), actuating on an NI-DAQ card (PCIe-6323; National Instruments, Austin, US).

Histology

For tissue collection, deeply anesthetized mice (Ketamine/Xylazine in saline, 180/24 mg/kg, i.p.) were transcardially perfused with phosphate buffered saline (PBS) and subsequently with 4% paraformaldehyde (PFA) in PBS. Upon perfusion, brains were explanted and post-fixed for at least 24h in 4% PFA. Brains were then embedded in agarose (3% in PBS), and coronal brain slices (50 μm thickness) were obtained using a vibratome. Slices were then incubated in DAPI in PBS for 5-10 min, and mounted on microscope slides using Fluoromount (*Serva*), before being imaged using an LSM 900 airyscan 2 confocal microscope (Zeiss, Germany) with a Plan-APOCHROMAT 20X/0.8 objective, controlled by the ZEN 3.1 imaging software. Finally, images were processed using *FiJi/ImageJ*.[93]

FFP recordings *in vitro*

Two weeks prior to the photometry recordings, slices were transduced either with rAAV2/9- CAG-NIR-GECO2 (1×10^{13} gc/ml) and rAAV2/9-hSyn-ChrimsonR-mCerulean (1.5×10^{12}, in the case of infrared indicator FFP configuration); or with rAAV2/9-hSyn-Grab-NE1h (9.9×10^{13} gc/ml) and rAAV2/9-hSyn-jRGECO1a (2×10^{13} gc/ml; for dual-color experiments) by adding 0.5 μL of viral suspension on top of each slice. For FFP measurements, the brain port of the FFC was placed above the slice at the point where fluorescence was highest in order to target fluorophore-expressing neurons. In the case of NIR-GECO2 experiments, an additional optical fiber (200 μm diameter, 0.22 NA) coupled to an orange laser (595 nm; Obis LS 100 mW; Coherent, Germany) for optogenetic stimulation was placed such that the whole slice was illuminated. In the case of dual-color experiments, 1 μL of (+)-Bicuculline (20 mM; 0130; Tocris) and L-norepinephrine hydrochloride (10 mM; 74,480; Merck Millipore, Germany) were subsequently added to the medium using a laboratory pipette.

FFP of inorganic fluorophores

Microscopy slides covered with the fluorophores Alexa 488, Alexa 546, and Alexa 647 were used as samples for the system characterization in the multi-color data acquisition mode. For this configuration, a combination of a 4-bandpass filter (440/20-521/21-607/34-700/45 nm; #87-239 Edmund Optics) and 500 nm long-pass filter (#62-976, Edmund Optics) was installed in the detector. To measure the spectrum of fiber auto-fluorescence and fluorophores, the photodetector was replaced with a spectrometer (CCS200/M; Thorlabs, Germany). As the Doric detector consists of two screwable parts, we have accommodated the emission filter into the input part of the detector, while replacing the part that contains the photodiode with an AD12F adaptor with FC connector (Thorlabs, Germany), connected to the spectrometer via an FC-SMA fiber cord (200 μm, 0.5 NA, FC-SMA; M129L01; Thorlabs, Germany). The spectrum of each fluorophore and fiber auto-fluorescence was then acquired during an exposure period of 5 s. Upon verification of the spectral components, we operated the modified PyPhotometry software in the 3-color mode, delivering sequential excitation light of 488/10 (FL488-10; Thorlabs, Germany), 548/10 (ET548/10x; Chroma, US), and 650/10 nm (FBH650-10; Thorlabs, Germany) while manually moving the 1.25 ferrule end of the coupler across microscopy slides covered with the fluorophores Alexa 488, Alexa 546, and Alexa 647.

Data analysis

All photometry data was acquired in *.ppd format.[53] Data analysis was performed with custom MATLAB scripts (MATLAB, The Mathworks, US). As a practically relevant measure, we used a bleaching and motion corrected signal $\Delta F/F$, calculated in a similar – but not exact same – way to Lerner et al.[10]: First, both the 405 and the 470 nm excited fluorescence traces were smoothed in a time window of 100 ms. Second, we fitted both the 405 and the 470 nm channels with a least-square polynomial fit (of from 2nd to 5th order, based on visual inspection; using MATLABs built-in "polyfit" function). We then divided signals by their respective fit in order to correct for

bleaching and bring both signals to the same scale. Finally, we calculated $\Delta F/F$ as the difference in fluorescence between the corrected calcium-dependent fluorescence (excited at 470 nm) and the corrected isosbestic fluorescence (excited at 405 nm):

$$\frac{\Delta F}{F} = \frac{F_{470\ nm}}{F_{470\ nm\ fit}} - \frac{F_{405\ nm}}{F_{405\ nm\ fit}}$$

In case of NIR-GECO2, we have calculated $\Delta F/F_0$ as the change in fluorescence of the active channel against its baseline fluorescence F_0 defined as the 10^{th} percentile of the smoothed and bleaching-corrected data trace:

$$\frac{\Delta F}{F_0} = \frac{F_{calcium} - F_0}{F_0}$$

QUANTIFICATION AND STATISTICAL ANALYSIS

Statistical tests were performed using custom-written MATLAB-scripts (see code availability). Correlation matrices for calcium activity, pupil size, and locomotion were calculated using Pearson's correlation coefficient. Welch's two-sample t-test was used for the comparison of the signal fluorescence levels and bleaching. Statistical details are reported in the corresponding sections of the manuscript. Throughout the manuscript, the following conventions for statistical significance are used: *: $p < 0.05$, **: $p < 0.01$, ***: $p < 0.001$, ****: $p < 0.0001$. As this manuscript presents proof of concept, neither randomization nor sample size estimation was performed.